

## REPORT DOCUMENTATION PAGE

Form Approved  
OMB No. 0704-0188

The public reporting burden for this collection of information is estimated to average 1 hour per response, including the time for reviewing instructions, searching existing data sources, gathering and maintaining the data needed, and completing and reviewing the collection of information. Send comments regarding this burden estimate or any other aspect of this collection of information, including suggestions for reducing the burden, to Department of Defense, Washington Headquarters Services, Directorate for Information Operations and Reports (0704-0188), 1215 Jefferson Davis Highway, Suite 1204, Arlington, VA 22202-4302. Respondents should be aware that notwithstanding any other provision of law, no person shall be subject to any penalty for failing to comply with a collection of information if it does not display a currently valid OMB control number.

**PLEASE DO NOT RETURN YOUR FORM TO THE ABOVE ADDRESS.**

1. REPORT DATE (DD-MM-YYYY) 1/Oct/2001	2. REPORT TYPE THESIS	3. DATES COVERED (From - To)		
4. TITLE AND SUBTITLE ANALYSIS OF THE 1998 SOUTHEAST ASIAN MONSOON AND THE DIURNAL RAINFALL CYCLE IN THE COUHT CHINA SEA		5a. CONTRACT NUMBER		
		5b. GRANT NUMBER		
		5c. PROGRAM ELEMENT NUMBER		
6. AUTHOR(S) CAPT MCLEOD RAYMOND S		5d. PROJECT NUMBER		
		5e. TASK NUMBER		
		5f. WORK UNIT NUMBER		
7. PERFORMING ORGANIZATION NAME(S) AND ADDRESS(ES) COLORADO STATE UNIVERSITY			8. PERFORMING ORGANIZATION REPORT NUMBER CI01-258	
9. SPONSORING/MONITORING AGENCY NAME(S) AND ADDRESS(ES) THE DEPARTMENT OF THE AIR FORCE AFIT/CIA, BLDG 125 2950 P STREET WPAFB OH 45433			10. SPONSOR/MONITOR'S ACRONYM(S)	
			11. SPONSOR/MONITOR'S REPORT NUMBER(S)	
12. DISTRIBUTION/AVAILABILITY STATEMENT Unlimited distribution In Accordance With AFI 35-205/AFIT Sup 1				
13. SUPPLEMENTARY NOTES				
14. ABSTRACT				
<b>DISTRIBUTION STATEMENT A</b> Approved for Public Release Distribution Unlimited			20011016 183	
15. SUBJECT TERMS				
16. SECURITY CLASSIFICATION OF: a. REPORT		17. LIMITATION OF ABSTRACT	18. NUMBER OF PAGES 65	19a. NAME OF RESPONSIBLE PERSON 19b. TELEPHONE NUMBER (Include area code)

COLORADO STATE UNIVERSITY

13 June 2001

WE HEREBY RECOMMEND THAT THE THESIS PREPARED UNDER OUR SUPERVISION  
BY RAYMOND SCOTT MCLEOD ENTITLED ANALYSIS OF THE 1998 SOUTHEAST ASIAN  
MONSOON AND THE DIURNAL RAINFALL CYCLE IN THE SOUTH CHINA SEA (SCS) BE  
ACCEPTED AS FULFILLING IN PART REQUIREMENTS FOR THE DEGREE OF MASTER  
OF SCIENCE.

Committee on Graduate Work

William M. Gray

Dennis L. Lynch

Richard T. John

Advisor

SF A - RS

Department Head

## **ABSTRACT OF THESIS**

### **ANALYSIS OF THE 1998 SOUTHEAST ASIAN MONSOON AND THE DIURNAL RAINFALL CYCLE IN THE SOUTH CHINA SEA (SCS)**

The onset and maintenance of the Southeast Asian monsoon (SEAM) has far-reaching implications for global circulation as well as the local welfare of a substantial portion of the world's population residing in Southeast Asia. Significant delay or premature onset can lead to extreme famine or flood, respectively. Before accurate prediction of the strength or weakness of any given monsoon, one must understand the fundamental structure and significant events that lead to the onset and how the monsoon maintains itself. Analysis of data from the 1998 South China Sea Monsoon Experiment (SCSMEX) has revealed fundamental structures and influences associated with the summer monsoon over this region. Comparison of SCSMEX data with independent data such as the Tropical Rainfall Measuring Mission (TRMM) has confirmed diurnal variations in rainfall over this region.

Raymond Scott McLeod  
Department of Atmospheric Science  
Colorado State University  
Fort Collins, Colorado 80523-1371  
Summer 2001

**THESIS**

**ANALYSIS OF THE 1998 SOUTHEAST ASIAN MONSOON AND THE  
DIURNAL RAINFALL CYCLE IN THE SOUTH CHINA SEA (SCS)**

Submitted by

Raymond Scott McLeod

Department of Atmospheric Science

In partial fulfillment of the requirements

for the Degree of Master of Science

Colorado State University

Fort Collins, Colorado

Summer 2001

## **ACKNOWLEDGEMENTS**

I would like to thank my advisor, Dr. Richard Johnson, for his patience and support throughout my research. His enthusiasm and dedication towards his students make him a joy to work for. I would also like to thank my committee members, Dr. William Gray and Dr. Dennis Lynch for their time and input. Paul Ciesielski was instrumental in guiding me through the fundamental frustrations of Fortran and I value his personal and professional mentorship greatly. Rick Taft kept my aging Sun station alive and provided several figures used in this study. Gail Cordova provided administrative help and her wonderful laugh often lightened the mood. Finally, I'd like to thank my officemate, Jim Kossin, for answering Unix questions, helping me understand more about Dynamics, and sharing his unique view of life.

The National Oceanic and Atmospheric Administration supported this research with grant NA67RJ0152. Salary and tuition were payed by the United States Air Force under the Air Force Institute of Technology Graduate Program.

The views expressed in this article are those of the author and do not reflect the official policy or position of the United States Air Force, Department of Defense, or the U.S. Government

## CONTENTS

<b>1</b>	<b>Introduction</b>	<b>1</b>
<b>2</b>	<b>Background</b>	<b>3</b>
2.0.1	1998 SEAM . . . . .	3
2.0.2	Diurnal Cycle . . . . .	4
2.0.3	Objectives of Study . . . . .	7
<b>3</b>	<b>Data and Analysis</b>	<b>8</b>
3.1	Data Description . . . . .	8
3.2	Analysis . . . . .	12
3.2.1	Mean State Analysis . . . . .	12
3.2.2	Method to Determine Apparent Moisture Sink and Precipitation by Line Integration . . . . .	12
3.2.3	Analysis of TRMM and SCSMEX Diurnal Precipitation Estimates . . . . .	14
3.2.4	Diurnal Moisture Convergence using SCSMEX Data for NESA . . . . .	14
<b>4</b>	<b>Results</b>	<b>16</b>
4.1	Mean State Analysis . . . . .	16
4.1.1	Streamline Analysis . . . . .	16
4.1.2	Divergence and Outgoing Longwave Radiation . . . . .	21
4.1.3	Conditional Stability . . . . .	23
4.2	Precipitation Measurements . . . . .	35
4.2.1	$Q_2$ Line Integration Rainfall Estimates Compared to TRMM Combined TMI/PR Estimates . . . . .	35
4.2.2	Monthly averaged, and Diurnally Computed NESA Precipitation Estimates . . . . .	37
4.2.3	Two-Month averaged, and Diurnally Computed SCSMEX and NESA Precipitation Estimates . . . . .	45
4.2.4	Diurnal Cycle of Heavy Precipitation, NESA . . . . .	56
<b>5</b>	<b>Conclusions</b>	<b>57</b>
5.0.5	Future Work . . . . .	58
<b>6</b>	<b>Appendix</b>	<b>60</b>
<b>7</b>	<b>References</b>	<b>62</b>

## FIGURES

1.1 SCSMEX/GAME sounding network. In this study the region from 10S–40N and 80–130E is considered the SCSMEX region. Colored dots indicate sounding site locations, number of soundings per day ranging from 1–4 times daily, and vertical resolution in millibars (mb) ranging from 5–100mb. . . . .	2
2.1 (Asai et al. 1998) Amplitude and phase of the diurnal variation of cloudiness over China derived by Fourier analysis for the April to June 1987. Each full barb and pennant represent 0.2 and 1.0 in amplitude of diurnal cycle variation of cloudiness, respectively. An arrow pointing from the North indicates a 0000 LST maximum and one pointing from the East indicates a 0600 LST maximum, etc. . . . .	6
3.1 Sounding network with northern and southern enhanced sounding arrays . . . . .	9
3.2 Typical TRMM overpass swaths approximately for TMI and PR with begin and end times of swath paths . . . . .	11
4.1 IOP1 850 mb streamlines, by pentad . . . . .	17
4.2 IOP2 850 mb streamlines, by pentad . . . . .	18
4.3 IOP1 200 mb streamlines, by pentad . . . . .	19
4.4 IOP2 200 mb streamlines, by pentad . . . . .	20
4.5 IOP1 200 mb divergence and OLR, by pentad. Solid contours are divergence and dashed contours are convergence, in increments of $5 \times 10^{-6} s^{-1}$ . . . . .	22
4.6 IOP2 200 mb divergence and OLR, by pentad. Solid contours are divergence and dashed contours are convergence, in increments of $5 \times 10^{-6} s^{-1}$ . . . . .	23
4.7 Time series of $\theta_e^*$ at <i>Kexue 1</i> during IOP1 . . . . .	24
4.8 Time series of $\theta_e^*$ at <i>Shiyan 3</i> during IOP1 . . . . .	25
4.9 500 mb streamlines and OLR for 7 May 1998 over the SE Asia region . . . . .	26
4.10 500 mb streamlines and OLR for 10 May 1998 over the SE Asia region . . . . .	27
4.11 500 mb streamlines and OLR for 15 May 1998 over the SE Asia region . . . . .	28
4.12 500 mb streamlines and OLR for 17 May 1998 over the SE Asia region . . . . .	29
4.13 Time series of relative humidity at <i>Shiyan 3</i> during IOP1 . . . . .	30
4.14 Daily precipitation at 4 stations during May 1–July 31, 1998. Stations are aligned from north to south, top to bottom, respectively. (Li and Wu, 1999) . . . . .	31
4.15 500 mb streamlines and OLR for 16 May 1998 over the SE Asia region . . . . .	32
4.16 500 mb streamlines and OLR for 18 May 1998 over the SE Asia region . . . . .	33
4.17 500 mb streamlines and OLR for 19 May 1998 over the SE Asia region . . . . .	34

4.18 Example of TRMM orbit swath and bounding polygon used in line integration. The hatched swath indicates the area covered by TRMM and start and end times, UTC. Note the approximate time difference of 1.3 hour delay between swath start and end times and sounding time. . . . .	36
4.19 Rain rate estimates for NESA region from European Centre for Medium-Range Weather Forecasting (ECMWF), Japan Meteorological Agency (JMA), Global Precipitation Climatological Project (GPCP), TRMM-3B42, and Q2-B $Q_2$ moisture budget precipitation estimates. Numbers to the right indicate total rainfall average estimates in mm/day. . . . .	38
4.20 May rain rates for TMI, PR, and moisture budgets from the NESA region . . . . .	39
4.21 June rain rates for TMI, PR, and moisture budgets from the NESA . . . . .	40
4.22 Moisture budgets with storage terms ( $dq/dt$ ), moisture convergence (MC), evaporation ( $E_o$ ), and precipitation ( $P_o$ ), May 1998, NESA. 0000 UTC = 0800 LST, etc. . . . .	41
4.23 Moisture budgets with storage terms ( $dq/dt$ ), moisture convergence (MC), evaporation ( $E_o$ ), and precipitation ( $P_o$ ), June 1998, NESA. 0000 UTC = 0800 LST, etc. . . . .	42
4.24 Divergence fields over NESA for 1-10 June 1998. Arrows indicate wind field. . . . .	43
4.25 Hong Kong wind rose at 850 mb, averaged from 1-10 June. . . . .	44
4.26 Diurnal oscillations of wind speed and direction at the maximum jet wind level for (a) southerly and (b) northerly LLJs. The U represents the eastward wind speed component and V the northward component. Indicated times are central standard time. Data collected over a two year period. (Whiteman et al. 1997) . . . . .	45
4.27 Rain rates in the NESA region for May and June 1998. . . . .	46
4.28 TMI and PR rain rates in the SCSMEX region for May and June 1998. . . . .	47
4.29 TMI and PR rain rates averaged in 3 hour intervals in the NESA region for May and June 1998. . . . .	48
4.30 TMI and PR rain rates averaged in 3 hour intervals in the SCSMEX region for May and June 1998. . . . .	49
4.31 Diurnal variation in rain rates from TRMM TMI for the SCSMEX region during May and June 98. Error bars represent one standard deviation. . . . .	50
4.32 Diurnal variation in rain rates from TRMM PR for the SCSMEX region during May and June 98. Error bars represent one standard deviation. . . . .	51
4.33 Diurnal variation in rain rates from TRMM TMI for the NESA region during May and June 98. Error bars represent one standard deviation. . . . .	52
4.34 Diurnal variation in rain rates from TRMM PR for the NESA region during May and June 98. Error bars represent one standard deviation. . . . .	53
4.35 Harmonic dials of diurnal precipitation for the (a) boreal summer and (b) wintertime for the Maritime Continent. They were calculated by averaging the amplitudes and phase of harmonic dial in polar coordinates for each day of the entire data period. Peak time can be read in local solar time as marked in the diagram below the lower left of (b). The eastward arrow indicates the hour of maximum occurred at 0000 LST. Phase in hour increases counterclockwise. The scale for the arrows is given in mm day <sup>-1</sup> below the bottom of each figure. The dials were drawn at every grid point to show detailed change of harmonic arrows in their magnitude and orientation. (Lim and Suh, 2000) . . . . .	54
4.36 As in Fig. 4.35, except for the semidiurnal component of the assimilated amounts of precipitation. (Lim and Suh, 2000) . . . . .	55

4.37 TMI, PR, and combined rain rates greater than 7.6 mm/hr over the NESA . . . . .	56
--	----

## **TABLES**

4.1	Rainfall estimates from TRMM combined rainfall estimates and sounding derived line integration rainfall estimates. . . . .	37
4.2	Rainfall estimates from TRMM TMI and PR algorithms and sounding derived moisture budgets, (MB) . . . . .	38
6.1	List of abbreviations and symbols . . . . .	61

## **Chapter 1**

### **INTRODUCTION**

Tropical convection has been described as the "firebox" for the Earth's heat engine. Riehl and Simpson (1979) stated that in the tropics, half of the incoming solar radiation absorbed by the top layers of the ocean is returned by evaporation to the atmosphere. Most of this latent heat is then released back into the atmosphere via deep tropical convection. This heat is carried poleward via the Hadley cell circulation and eventually serves to warm the higher latitudes. Much of the tropical convection happens during the Asian and Indian summer monsoons. The importance of the monsoons and their impact on the global circulation cannot be underestimated.

In addition to the impact tropical convection has on global heat distribution, the onset and maintenance of the Asian monsoon has a direct impact upon a region that contains a substantial part of the Earth's population. A weak or strong Asian monsoon can mean famine or flood to the people of Southeast Asia. Advances in understanding the onset and maintenance of the monsoon can lead to better forecasting. This in turn can help world organizations and local governments plan for the subsequent consequences of a strong or weak monsoon.

The South China Sea Monsoon Experiment (SCSMEX), 1 May-30 June 1998, was an international field experiment with goals of understanding the onset and maintenance of the Southeast Asian and South China monsoons. Figure 1.1 depicts the entire SCSMEX GEWEX Asian Monsoon Experiment (GAME) region. Intensive meteorological observations were taken using various platforms and techniques which are described by Lau et al. (1999). Preliminary results from this paper indicated significant influences from midlatitude synoptic waves and tropical convection that

induced the onset of the South China Sea monsoon.

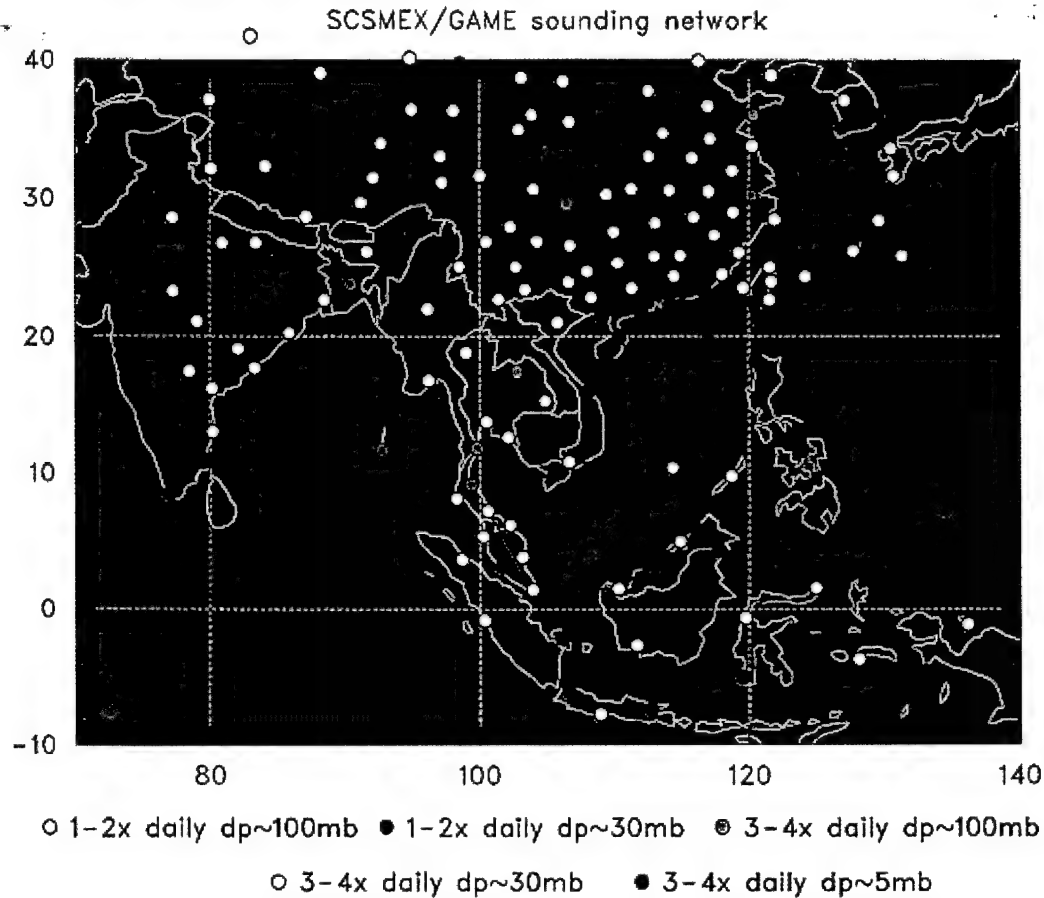


Figure 1.1: SCSMEX/GAME sounding network. In this study the region from 10S–40N and 80–130E is considered the SCSMEX region. Colored dots indicate sounding site locations, number of soundings per day ranging from 1–4 times daily, and vertical resolution in millibars (mb) ranging from 5–100mb.

In order to examine these and other characteristics of the SCS monsoon, an overview of some of the synoptic conditions are examined within this paper. Streamline and divergence analysis combined with independent outgoing longwave radiation (OLR) data revealed lower- and upper-level structure during the two-month observation period. Tropical Rainfall Measuring Mission (TRMM) data and gridded sounding data helped to diagnose diurnal variations in rainfall over the northern SCS.

## **Chapter 2**

### **BACKGROUND**

This chapter will describe the background for this study, including general characteristics of the 1998 Southeast Asian Monsoon (SEAM) and some of the work on the diurnal rainfall and wind cycle.

#### **2.0.1 1998 SEAM**

The extensive data set obtained during SCSMEX prompted many articles on the analysis of the 1998 Asian monsoon and the onset date for the SCS. The onset dates range from 15 May for the northern SCS and 20 May for the southern SCS (Johnson et al. 1999) to 21 May and 25 May for the entire SCS (Li and Wu 2000; Chan et al. 2000). All of these dates are based on different interpretations of the onset of the monsoon. Without advocating one method over another, for this study the onset period of the monsoon in the northern SCS is 15-17 May and for the southern SCS it is 20-25 May (Lau et al. 2000).

In general, convection over the SCS starts in mid-April along the Borneo-Malaysia-Indo-China land bridge. It then skips over the majority of the SCS to form the Mei-Yu and Baiu front that produces rainfall from central China to Japan (Johnson et al. 1998). After the Mei-Yu/Baiu front is established, convection breaks out over the entire SCS. Prior to forming the fronts mentioned above, the atmosphere must be primed for convection and the dominant low-level easterlies must be replaced by the southwesterly monsoonal flow.

An integral part of the evolution of the 1998 Asian monsoon is the tropical depression that

first appeared in the Bay of Bengal around 12 May (Chan et al. 2000). Krishnamurti et al. (1981) described an onset vortex for the Arabian Sea as a major contributing factor for the Indian monsoon. The cyclone identified by Chan et al. served several purposes in helping to initiate the SCS monsoon. It replaced the dominant easterly flow with southwesterly flow across the Indochina peninsula and also initiated cross-equatorial flow near Borneo. This primed the atmosphere with moisture and heat from the equator and southern hemisphere needed for convection.

Once the vortex had primed the atmosphere, a triggering mechanism was needed to set off convection. Midlatitude fronts and troughs have been recognized as such a triggering mechanism (Chang 1995). Loechl (2001) suggested the importance of the convergence of the Madden-Julian Oscillation and a midlatitude frontal zone to initiate the monsoon.

### 2.0.2 *Diurnal Cycle*

In general, the literature agrees that oceanic tropical rainfall (notably heavy rain events) has an evening to mid-morning maximum (local time) and a late afternoon (local time) minimum. Ruprecht and Gray (1976a,b) and Gray and Jacobson (1977) were the first to elucidate this fact to the scientific community. They found that morning rainfall was 250% more than evening rainfall associated with active cloud clusters in the western Pacific (Ruprecht and Gray 1976a,b). Gray and Jacobson furthered these results by linking the strength of the cloud clusters to the strength of the diurnal cycle they reflect. Chen et al. (1996) also confirmed this using satellite-derived cloud top temperatures.

Several theories have been proposed to explain the mid-morning maximum in oceanic rainfall. Ruprecht and Gray (1976) postulated day-versus-night radiation subsidence (DNS) as the primary mechanism for morning convection. Essentially, longwave tropospheric cooling is balanced during the day by shortwave radiational warming. At night, cooling increases and compensating large scale subsidence takes place. The subsidence in clear areas is mass balanced by convergence in and around the cloud clusters and convection is increased. Direct radiative cloud forcing (RCF)

has most recently been explained by Xu and Randall (1995a,b). This process depends upon destabilization of cloud tops by nocturnal cooling, cloud base destabilization by absorption of longwave radiation from adjacent clouds or the surface, and daytime stabilization of cloud tops by solar heating. All of these processes serve to form a morning maximum in convection in the tropical ocean environment.

Other studies have identified diurnal cycles that are seasonally and location dependent. Dai and Desser (1999) used three-hourly wind observations from around the globe to analyze global wind and surface observations. They found land and adjacent oceanic area diurnal wind anomalies to be out of phase with each other. The maximum divergence over land was noted between 0600-0800 local standard time (LST) and the maximum divergence over the oceanic region was found to be 1700-1900 LST. This relationship was also found to be reversed in the early morning with maximum convergence over water and maximum divergence over land.

Recently Krishnamurti and Kishtawal (1999) identified a diurnal pulsing of the Tibetan anticyclone. They noted that the velocity potential field at 200 mb centered over India displayed an outflow at 1800 LST and an inflow at 0600 LST. This outflow and a descending divergent lobe of the anticyclone stretches from the SCS to the Arabian Sea. In this same study, TRMM data were used to examine the diurnal signal. Although only fourteen days of data were used, the results indicated a strong convection over central India at 1800 LST. They demonstrated that the pulsation of the anticyclone reaches far from its source. Does this pulsation aloft affect convection over the SCS? If the flow in the anticyclone does in fact converge during the morning over central India, is there compensating morning divergence aloft over the SCS?

Asai et al. (1998) demonstrated that diurnal variations in cloudiness result from superposition of diurnal-cycle and small semidiurnal-cycle variations. Figure 2.1 shows that, during the warm season, the northern SCS exhibits an afternoon maximum in cloudiness. Does this also mean that the maximum convection also occurs in the afternoon?

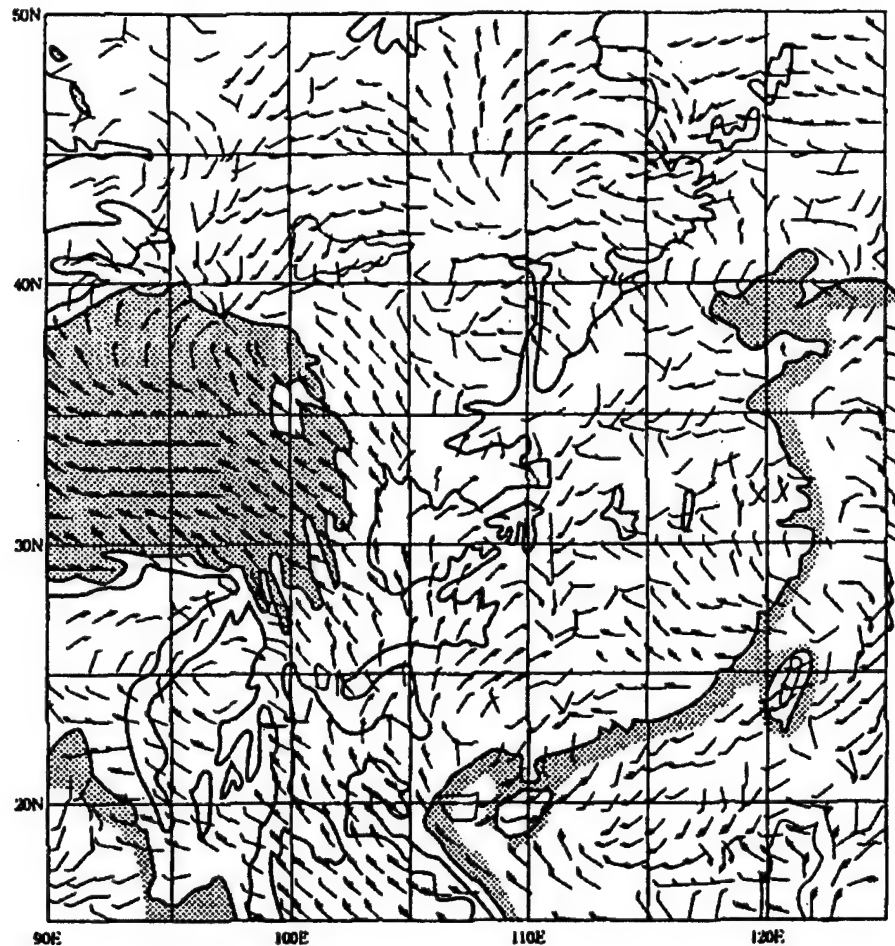


Figure 2.1: (Asai et al. 1998) Amplitude and phase of the diurnal variation of cloudiness over China derived by Fourier analysis for the April to June 1987. Each full barb and pennant represent 0.2 and 1.0 in amplitude of diurnal cycle variation of cloudiness, respectively. An arrow pointing from the North indicates a 0000 LST maximum and one pointing from the East indicates a 0600 LST maximum, etc.

Local diurnal signals can be heavily influenced by terrain. Chen et al. (1999) demonstrated that all island Taiwan rainfall showed semidiurnal signals of a morning minor maximum and an early evening primary maximum. They attributed the early morning maximum to drainage flow off of the Taiwan central mountain range and convergence with the southwesterly monsoonal flow. Here the large scale low-level flow interacts with local features to create a bimodal distribution in rainfall.

### **2.0.3      *Objectives of Study***

In summary, this study is directed toward examining the large scale features of the 1998 SCS monsoon and conditions leading up to the onset. TRMM data and moisture budget data are used to examine and compare diurnal signals of rainfall. Some questions the author examines are:

- What were the larger-scale conditions and their variability during the SEAM?
- What diurnal rainfall signal is present over the northern SCS, and what signal is present over the larger SCSMEX region?
- How do TRMM measurements of the diurnal rainfall pattern over the northern SCS compare with atmospheric budgets?

## **Chapter 3**

### **DATA AND ANALYSIS**

The purpose of this chapter is to describe the data sets used in this study and to explain the method used in analyzing the data

#### **3.1 Data Description**

The primary sounding data used in this study were collected in May-June 1998 from the sounding network of the South China Sea Monsoon Experiment (Global Energy and Water Cycle Experiment (GEWEX)) Asian Monsoon Experiment (GAME). The sounding network was established in the South China Sea to investigate the onset and development of the East Asian monsoon. For this study soundings were analyzed for the area encompassing 40N-10S and 80E-130E.

Two Intensive Observing Periods (IOPs) (5-25 May and 5-25 June) were conducted which involved two research vessels, *Kexue 1* and *Shiyan 3*, as well as other island and coastal stations. Typically six-hourly soundings were obtained during these IOPs. The Northern Enhanced Sounding Array (NESAs) is centered near the *Shiyan 3* at 20N and 117E and is shown in 3.1. The Southern Enhanced Sounding Array is also shown in 3.1 and is centered near the *Kexue 1 #1* at 6N and 110E.

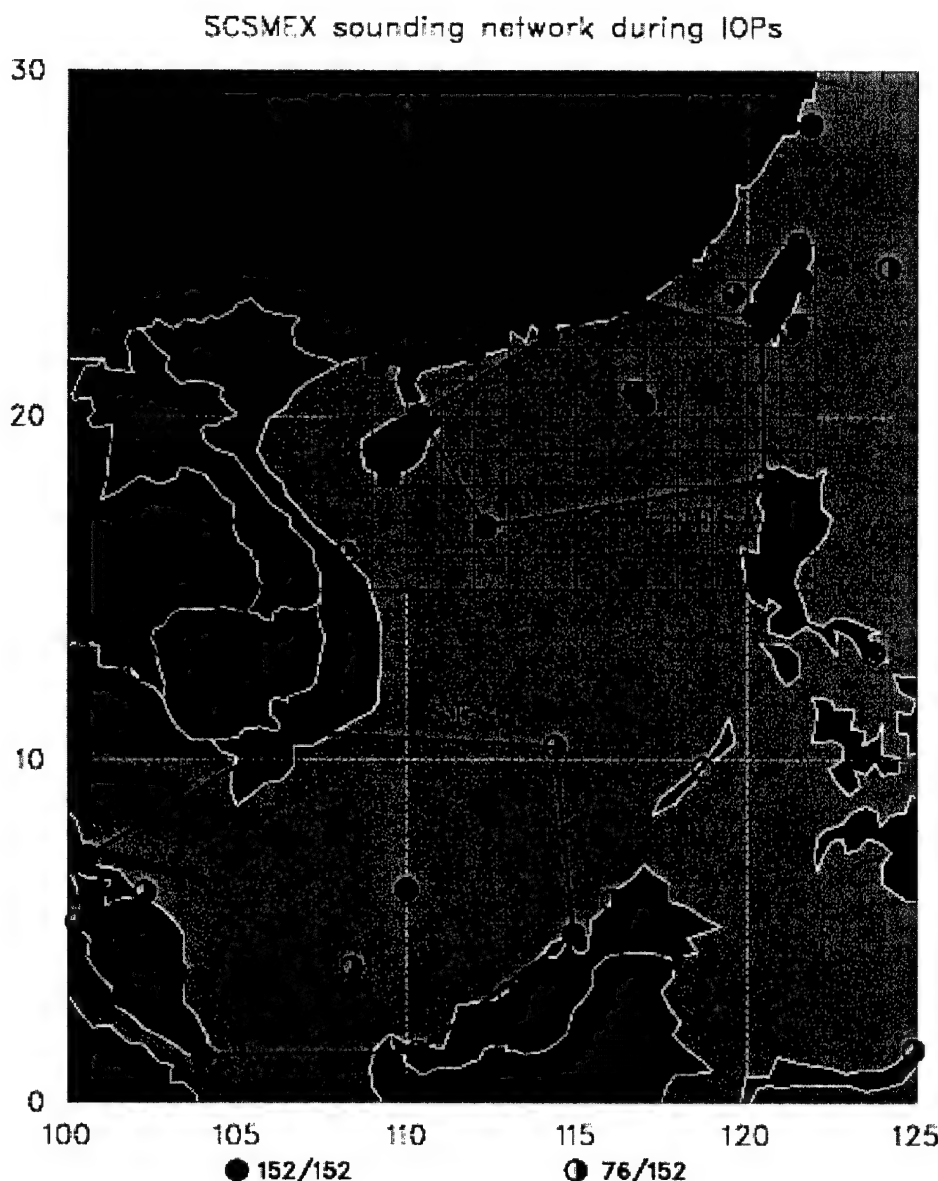


Figure 3.1: Sounding network with northern and southern enhanced sounding arrays

The SCSMEX sounding data were decoded and quality controlled by Paul Ciesielski at Colorado State University. Results for the NESA polygon were obtained from a gridded array covering 25-15N and 108-122E. The resolution of the grid is ( $1^{\circ} \times 1^{\circ}$ ) and the effectual resolution is dependent upon the distance between sounding stations. The gridding procedure used multiquadradic

(MQD) interpolation which uses radial basis functions that are circular hyperboloids as described in Hardy (1990). Nuss and Titley (1994) showed MQD interpolation to be more accurate than traditional Barnes (1964) scheme. The MQD interpolation retains large scale features over data sparse regions and includes smaller features within data rich regions.

Data from the Tropical Rainfall Measuring Mission (TRMM) satellite was obtained via <ftp://aeolus.nascom.nasa.gov/pub>. The 3G68 data were used (Kummerow et al. 2000). This set included rainfall estimates from the 2A12 TRMM Microwave Imager (TMI) algorithm , the 2A25 precipitation radar (PR) algorithm, and the 2B31 combined radar radiometer algorithm,. Mean rain rates, given in mm/hr, from this data set were used in this study. Minimum detectable rainfall rates for the PR and TMI have been stated at  $\geq$  0.2-0.4 mm/hr (Schumacher and Houze 2000) and  $\geq$  0.5 mm/hr (personal communication Dr. Christian Kummerow), respectively. Omission of values below these threshold values changes the averaged values very little. Additionally, Kummerow (2000, personal communication) suggests an error range for averaged readings for both the TMI and PR. The true rainfall rate for a large region can be within plus 20% or minus 5% from the PR estimates and; minus 20% and plus 5% of the TMI estimates.

The TRMM data are stored on a universal grid from 90S, 180W to 90N, 180E. These points correspond to array values of (0,0) and (360, 720) respectively on a ( $0.5^\circ$ x  $0.5^\circ$ ) grid. TRMM only collects data from approximately  $38^\circ$ S to  $38^\circ$ N, therefore all data north and south of these latitudes are set to zero. This selection of the universal grid allows integration and manipulation of data from other satellite platforms that collect data outside TRMM's collection region.

The effective footprint, or effective field of view (EFOV) of the orbital scan swath for the TMI is 759 km and the EFOV of the PR is 215 km. As evident from Fig. 3.2 the EFOV does not provide complete coverage over the entire region for a given day or time. Since very little TRMM data matches the exact times of synoptic rawinsondes, a decision was made to collect TRMM data which would most closely represent the synoptic times of interest. To match sounding derived data to TRMM data, and detect any diurnal signal present, times of interest are centered on standard

synoptic observation times and binned in intervals of six hours or less.

Capturing an accurate diurnal signal from the TRMM data requires more than the two month time frame examined in this study. Many years of data collection are required in order to exclude anomalies. However, for this study, two months of data does provide an indication of the diurnal signal over the given regions, and is an independent source against which other estimates may be compared.

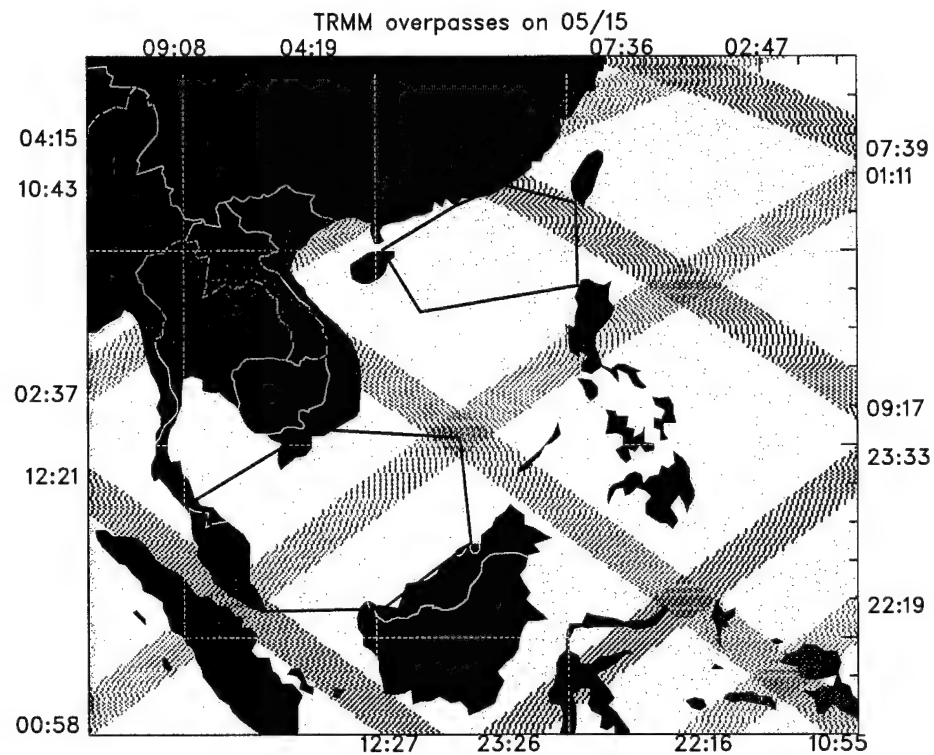


Figure 3.2: Typical TRMM overpass swaths approximately for TMI and PR with begin and end times of swath paths

Rain gauge data are used from Dongsha Island, located near the center of the NESA at 20°N and 116°E, to compare diurnal patterns of TRMM and sounding derived rainfall estimates. Data were collected from a tipping bucket rain-gauge that recorded once per minute in millimeters. These data were binned into six-hourly intervals centered on 02, 08, 14, and 20 local time for comparison

with the other rainfall estimates.

### 3.2 Analysis

#### 3.2.1 Mean State Analysis

General analysis was performed in order to understand the basic synoptic state of the onset and generally activity of the monsoon. Streamlines were used at several layers to understand the general flow aloft and surface to 700 mb. In order to roughly judge the accuracy of the SC-SMEX data, Outgoing Longwave Radiation (OLR) were used to match areas of cold cloud tops and maximum divergence aloft and convergence near surface. Fields of conditional stability were also analyzed to understand when conditions were ripe for active phases or inactive phases. Additionally, divergence and OLR fields were examined on a twice daily basis and animated to see if obvious synoptic features were revealed.

Analysis of the basic state helped define active areas for further examination by the following methods.

#### 3.2.2 Method to Determine Apparent Moisture Sink and Precipitation by Line Integration

A line integration technique was employed by selecting three or more sounding sites and computing moisture budgets within the area encompassed by the sites. Horizontal divergence was linearly adjusted by the method outlined in O'Brien, (1970). In this procedure vertical motion was set to zero at the tropopause (analyzed to be at roughly 100 mb). The parameter  $Q_2$ , the apparent moisture sink (Yanai, et al, 1973) is used to determine the precipitation estimates.  $Q_2$  is defined by

$$Q_2 \equiv -L \left( \frac{\partial \bar{q}}{\partial t} + \mathbf{v} \cdot \nabla \bar{q} + \bar{\omega} \frac{\partial \bar{q}}{\partial p} \right). \quad (3.1)$$

The equation above uses standard notation where  $L$  is the latent heat of condensation,  $q$  the mixing ratio of water vapor,  $\mathbf{v}$  the horizontal wind,  $\omega$  the vertical pressure velocity, and  $\nabla$  is the isobaric

gradient operator. The overbar denotes a grid-scale average.  $Q_2$  can be interpreted as

$$Q_2 \equiv L(c - e) + L \frac{\partial}{\partial p} \overline{q' \omega'} \quad (3.2)$$

where  $c$  is the rate of condensation per unit mass of air and  $e$  is the rate of re-evaporation of cloud and rain water. The primes denote deviations from the mean state. The last term on the right hand side of equation 3.2 is defined as the vertical eddy flux of moisture due to turbulent and convective motions. Assuming that vertical motion and moisture are negligible at the tropopause, the last term, vertically integrated, yields the surface evaporation.

By integrating  $Q_2$  from the tropopause  $p_t$  to the surface pressure  $p_s$ , we obtain

$$\langle Q_2 \rangle = L(P - E) \quad (3.3)$$

where  $\langle \cdot \rangle \equiv \frac{1}{g} \int_{p_t}^{p_s} (\cdot) dp$  and  $P$  and  $E$  are the precipitation rate and evaporation rate per unit area at the surface.

To evaluate precipitation rates from  $Q_2$  we need to estimate  $E$  and vertically adjust  $\omega$ . In order to set an upper limit to the vertical motion, diagnosis of the tropopause height was necessary. Several soundings were examined for average tropopause during the investigative period. After examining several soundings, 100 mb was determined as a representative pressure surface for the tropical tropopause. Precipitation rates varied little with changes in tropopause height of plus or minus 50 mb. Therefore the representative tropopause height was selected at 100 mb. The evaporation estimates were obtained from ECMWF operational analysis. So solving for  $P$  above we have

$$P = \frac{\langle Q_2 \rangle}{L} + E \quad (3.4)$$

Computations of  $P$  are sensitive to sampling errors, data errors, and errors introduced by analysis schemes. Since the sampling errors are mostly random, precipitation estimates obtained by this method become more reliable as the averaging period is increased. These budget methods work

best during periods of strong forcing. During periods of subsidence errors can result in negative precipitation rates. Therefore this procedure was primarily used in periods of strong forcing or over long time periods in order to minimize these problems.

Line integration areas involving subsets of the soundings in the NESA (Fig. 3.1) were selected to coincide with strong forcing regions and compared to TRMM overpasses that were sampled close to standard rawinsonde times. Average precipitation rates were obtained from the line integration technique and TRMM overpasses and compared to one another. TRMM data were selected to roughly match the same area as the representative polygon established by the rawinsonde sites used for in the line integration technique.

### *3.2.3 Analysis of TRMM and SCSMEX Diurnal Precipitation Estimates*

Two regions were used to evaluate average rain rates, the SCSMEX region (Fig. 1.1) and the NESA. TRMM data were filtered to match the two areas. Then TRMM data were binned into four time intervals centered on standard rawinsonde times 00, 06, 12, and 18 universal coordinated time (UTC). Schumacher and Houze (2000) noted the problems of matching TRMM data with significant rain events over the Kwajalein oceanic validation site. These problems were due to the intermittent coverage the TRMM's presessional orbit creates and matching significant rain events with TRMM data. However, they also stated that the TRMM's presessional orbit made the data useful for measuring the diurnal cycle.

The precipitation estimates from the TRMM TMI and PR were compared to moisture budget estimates over the NESA only. Two-month mean and monthly mean diurnal cycle estimates are examined.

### *3.2.4 Diurnal Moisture Convergence using SCSMEX Data for NESA*

Moisture convergence over the NESA grid was determined by

$$\frac{1}{A} \int_{sfc}^{100} \int \int \nabla \cdot \mathbf{V} q dAdp, \quad (3.5)$$

where  $A$  is the NESA area. By the divergence theorem this becomes

$$\frac{1}{A} \int_{sfc}^{100} \oint \mathbf{V} \cdot \mathbf{n} dldp \quad (3.6)$$

Here the  $\mathbf{n}$  is the outward normal vector and  $dl$  is the boundary of the NESA. By assuming that the vertical velocity is zero at the surface and at 100 mb, moisture convergence is determined by the flux of moisture through the sides of the volume. By using the initial gridded data, the divergence is unadjusted. However, in order to achieve results consistent with a mass-balanced state, the horizontal velocities must be adjusted (Molinari and Skubis 1988). This has been done for the gridded fields using a relaxation technique developed by Ciesielski (2001, personal communication).

Moisture convergence was analyzed over the two-month SCSMEX period for the NESA region. These times were also analyzed for diurnal variations. Included in these analyses were moisture storage, evaporation, and diagnosed precipitation estimates from  $Q_2$  as described earlier. The moisture storage term is computed by center differencing the data over twelve hours.

An afternoon drying was noted in the moisture storage term. The amplitude of this drying was suspected to be caused by radiational heating of the moisture sensor, particularly at the Chinese stations, as described by Cole (1993). This problem was also described by Betts et al. (1994) in which he noted that this effect is not a true diurnal phenomenon. Although some sites that exhibited these features were eliminated, the impact on the calculation of the diurnal cycle is not known.

## **Chapter 4**

### **RESULTS**

The purpose of this chapter is to describe the mean state of the atmosphere contained within the 1998 SCSMEX data.

#### **4.1 Mean State Analysis**

##### **4.1.1 Streamline Analysis**

A general analysis of fundamental properties of the 1998 SCS monsoon is useful in order to understand the mean state of the atmosphere during the two month period of interest. Streamline analysis is probably the most basic technique used in tropical analysis for understanding general confluence and diffluence.

Analysis of the wind field using (five-day) pentad averaging reveals significant characteristics associated with the SEAM. The initial period of 1-5 May shows low-level anticyclonic rotation in the Bay of Bengal (BOB), easterly flow confined to 10N-10S, and the presence of the Western Pacific Subtropical Ridge (WPSR) nosing into the Indochina peninsula (Fig. 4.1). The 11-15 May pentad data shows a cyclonic circulation intensifying and moving into the BOB, displacing the anticyclonic activity noted earlier. A definite shift in the prevailing easterlies has taken place over the Indochina peninsula associated with the cyclonic center as it moves into the BOB over the 16-20 May period. The easterlies have shifted to southwesterlies and the influence of the WPSR has moved off the Indochina peninsula over the SCS. By the next pentad period, 21-25 May, west-

southwesterly flow dominates the majority of the peninsula while cross-equatorial flow is present over Borneo. Troughing is noted over the east coast of India and into the BOB and low-level ridging is present over northern Indochina and south along the Indochina peninsula. This ridging seems to be induced by the trough to its west and the cyclonic rotation over the Southeast China coast. This overall pattern changes little over the last pentad period, 26-30 May, except for the development of the trough over northern Indochina and extending into the SCS. Additionally, the cross-equatorial flow near Borneo has developed into a low-level anticyclone, cutting off convection into the southern part of the SCS.

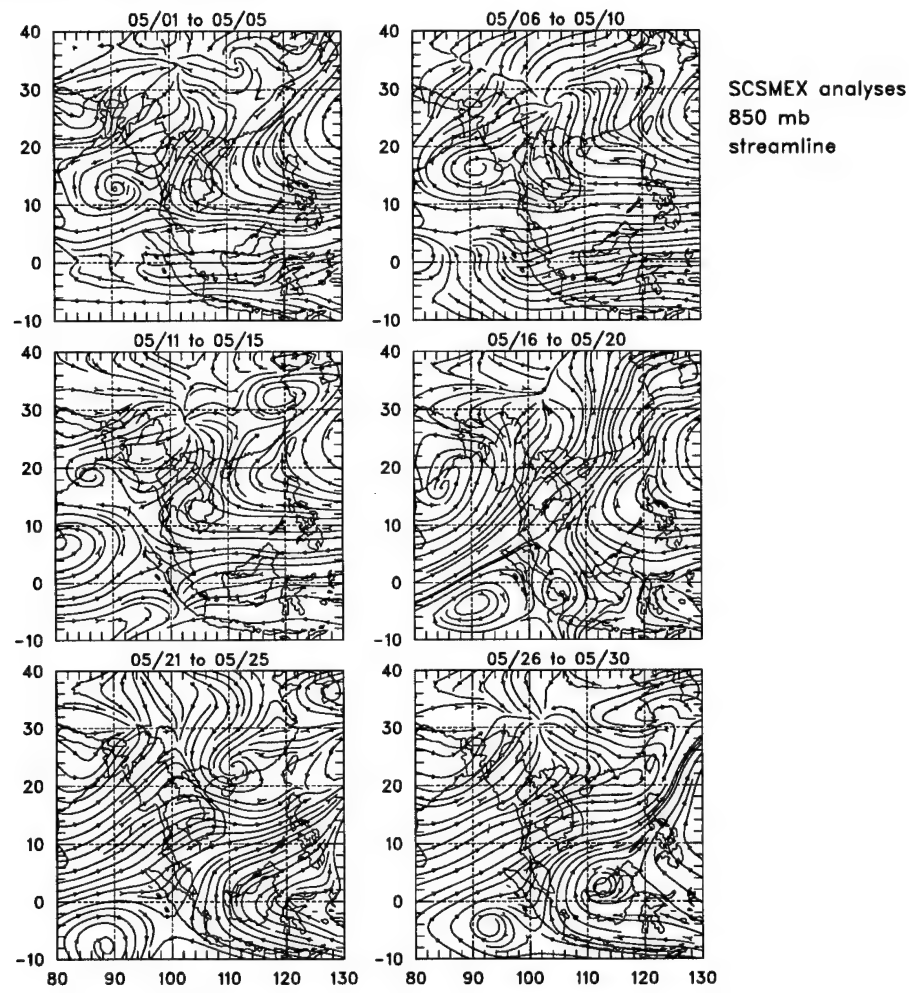


Figure 4.1: IOP1 850 mb streamlines, by pentad

The 850 mb streamlines during IOP2 show distinct southwesterly monsoonal flow over the Indochina peninsula (Fig. 4.2). A hypothetical convergence zone appears over the eastern Tibetan plateau, hypothetical in the sense that the topography lies well above the 850 mb surface. The influence of the WPSR is evident in every panel and the western extent of the WPSR extends significantly northward and westward in the last panel. This period is associated with easterly advection of dry air and suppressed precipitation.

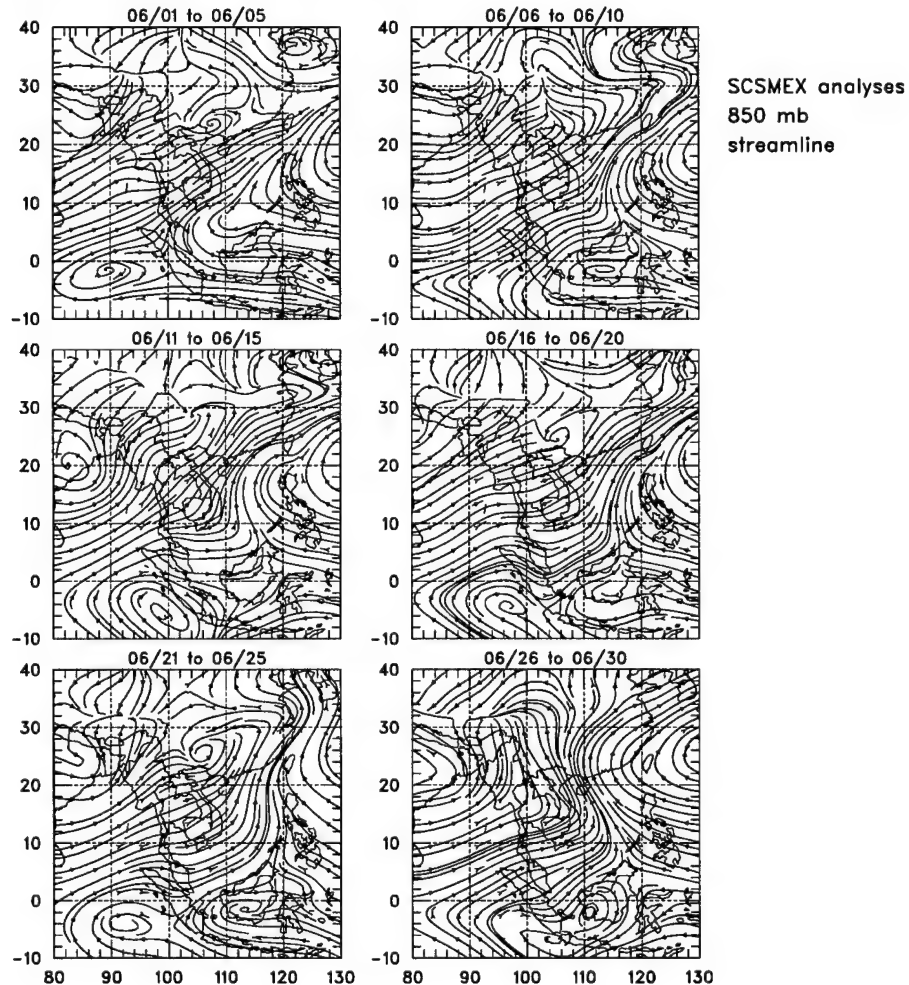


Figure 4.2: IOP2 850 mb streamlines, by pentad

The 200 mb streamline analysis (Fig. 4.3), for IOP1 is characterized by westerly flow transforming into ridging over the SCS and finally becoming a closed anticyclonic circulation over the

Indochina peninsula. This closed circulation is the first stage of the Tibetan High. The development of the Tibetan High was documented by Krishnamurti (1979) and Murakami and Nakazawa (1985) as starting in the SCS in April and migrating to Indochina in May and then to the Tibetan Plateau by July. Our data set reveals diffluent flow over the Indochina peninsula for the first pentad in May. The diffluent flow develops into ridging covering the Indochina peninsula for the second pentad in May. By the third pentad an anticyclonic center is evident over the eastern BOB which moves east over Indochina and stays centered there for the next four weeks.

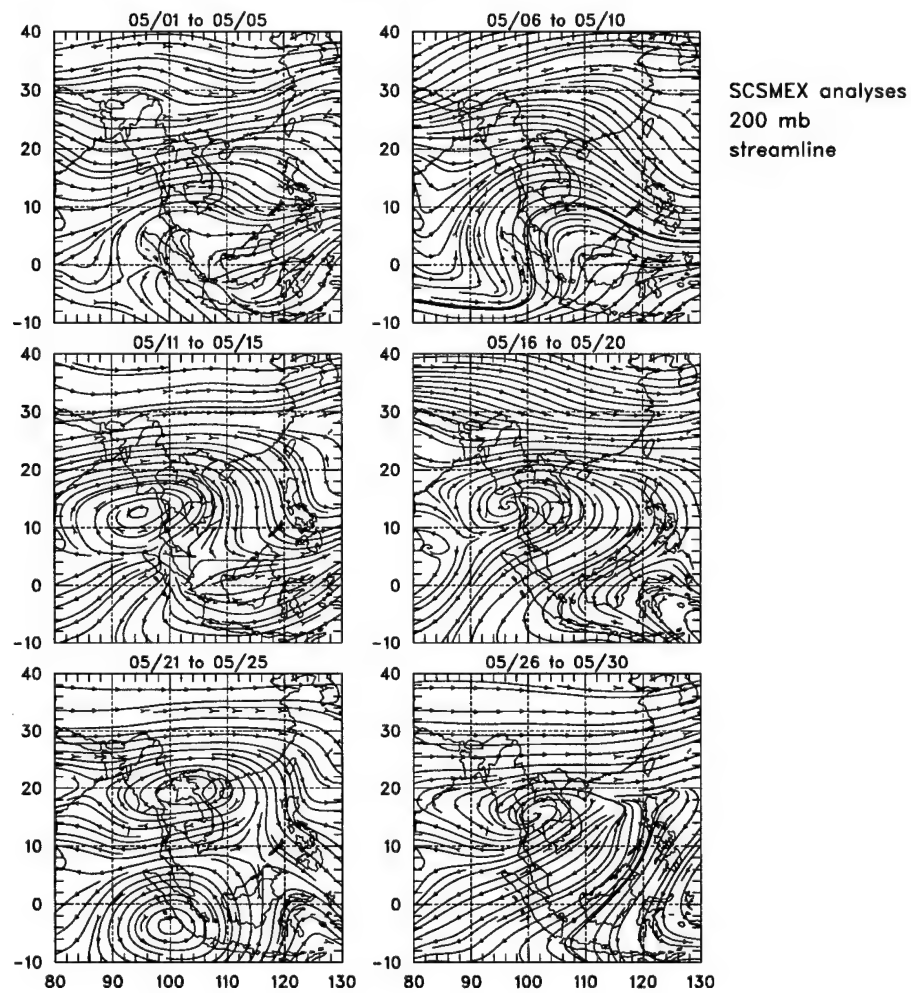


Figure 4.3: IOP1 200 mb streamlines, by pentad

As a side note, in IOP1 the 21-25 May pentad analysis shows an anticyclonic center in the

southern hemisphere near Sumatra. By examining satellite imagery, it was determined that this anticyclonic center is associated with a cloud cluster with a life span of about four days.

Streamline analysis at 200 mb during IOP2 (Fig. 4.4), is dominated by the large anticyclone over southeast Asia. As described by Krishnamurti (1979) and Murakami and Nakazawa (1985), it migrates northwestward, finally settling over the Tibetan plateau in mid-to-late June. Northerly cross-equatorial flow is distinctly present in every pentad in June. Another notable feature is the anticyclonic rotation evident in several panels near 10S. Satellite data show that during the first pentad of June, organized convection exists near Borneo and Sumatra. The final pentad of June indicates a possible TUTT (tropical upper tropospheric trough) to the east of the Philippines. Satellite imagery indicates significant convective activity to the west of the Philippines which may be associated with the upper-level cyclonic turning.

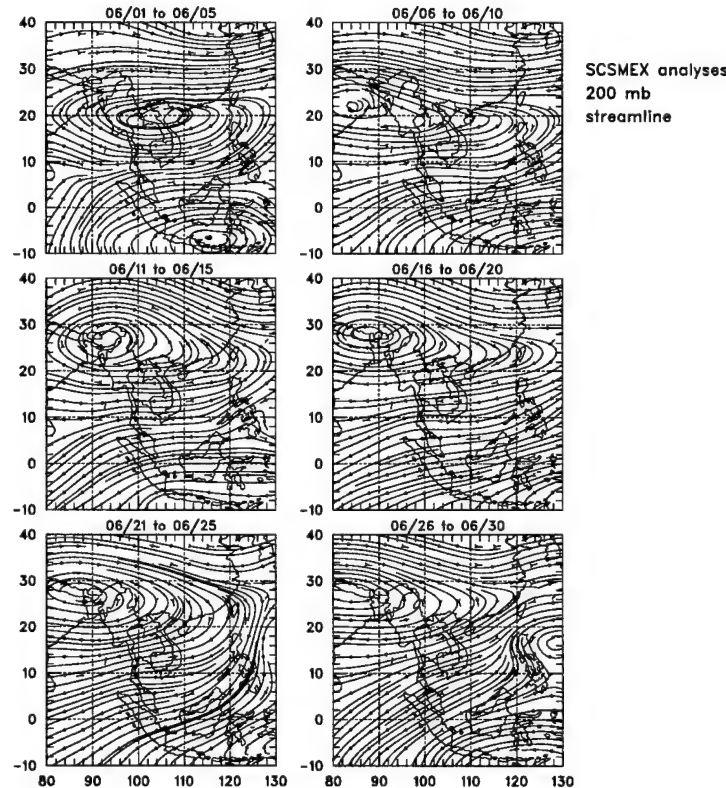


Figure 4.4: IOP2 200 mb streamlines, by pentad

#### **4.1.2 Divergence and Outgoing Longwave Radiation**

The previous streamline analyses depict diffluent and confluent centers which are closely correlated with convergent and divergent areas within the SCSMEX region. Using outgoing longwave radiation (OLR) from an independent data source gives one a sense of agreement between convergent and divergent areas. In the following cases darker or lighter areas are associated with low or high levels of OLR, respectfully. Lower values of OLR indicate high level clouds. In general, matching areas of maximum divergence aloft, convergent areas at lower levels and minimum radiative flux (low OLR), one can conclude that the data are generally in agreement with physical relationships in the atmosphere.

Examining IOP1 (Fig. 4.5), first pentad, a band of convergence and high OLR exists over the northern Indochina peninsula and over the Philippines. Both areas of upper-level convergence agree well with the higher OLR values. The convergent area over the Philippines is present until the onset of the monsoon, indicating the influence of the WPSR. Also, during the first and third pentads, a diagonal band of divergence and moderate OLR stretches from northern Vietnam to the northern SCS. These represent stalled synoptic frontal boundaries that help to induce convection.

During the fourth pentad, agreement is noted between low OLR and upper-level divergence stretching from the northern SCS across the Indochina Peninsula and into the BOB. This is consistent again with the stalled midlatitude fronts (referred to as the Meiyu front in China and the Baiu front in Japan) in the northern SCS and the cyclonic activity noted earlier in the BOB. The combination of these two features initiates the onset of the 1998 SCS monsoon (Loechl 2001). The cyclonic activity in the BOB helped to reverse the low-level flow over the SCS and increase low-level humidities. The stalled frontal region, as seen in the next section, provided upper-level instability needed to start convection.

Looking into the onset period, 21-25 May, one notes four areas that show agreement between OLR and 200 mb divergence. In the northeast corner of the region, an area of upper-level divergence and low OLR exists. Directly to the south of this area, an area of convergence and high OLR

is matched with another area of upper-level divergence and low OLR to its south. Upper-level divergence west of Sumatra is also represented well with low OLR values.

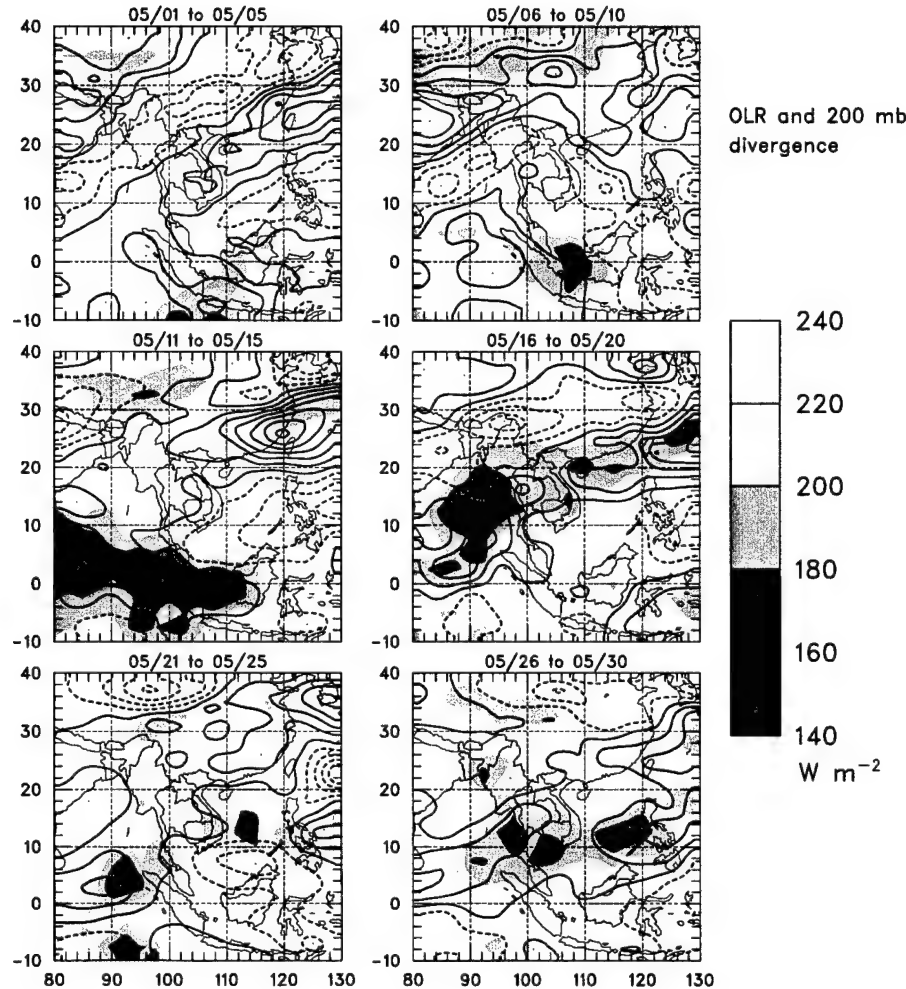


Figure 4.5: IOP1 200 mb divergence and OLR, by pentad. Solid contours are divergence and dashed contours are convergence, in increments of  $5 \times 10^{-6} s^{-1}$ .

Examining Fig. 4.6, the first pentad period in June, one finds that over the BOB and north of the Philippines, upper-level divergence coincides with low values of OLR. The second pentad continues to display the marked characteristics of the Mei-Yu/Baiu front with associated low OLR values. Convergent areas with high OLR values are noted on both sides of the frontal zone near Taiwan. The third pentad in June is marked by a break period in the monsoon with convergent areas

over most of China and the Mei-Yu front farther north. The fourth pentad is once again consistent with the divergence associated with the front and convergence behind it. The fifth and sixth pentads also show agreement as a majority of the area is dominated by upper-level divergence and low OLR.

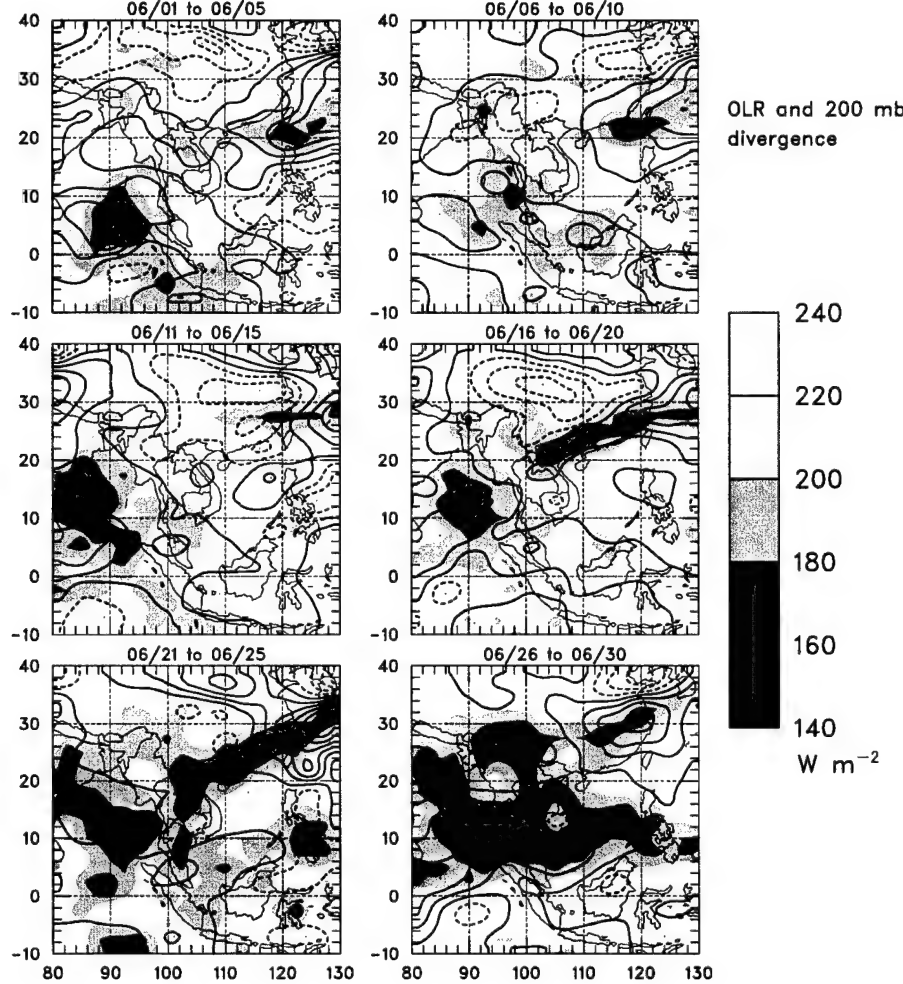


Figure 4.6: IOP2 200 mb divergence and OLR, by pentad. Solid contours are divergence and dashed contours are convergence, in increments of  $5 \times 10^{-6} s^{-1}$ .

#### 4.1.3 Conditional Stability

In order to identify periods favorable for convective activity, the saturated equivalent potential temperature  $\theta_e^*$  was examined at several sites. The vertical structure of  $\theta_e^*$  can help diagnose

possible origins of instability. The use of  $\theta_e^*$  makes tropopause heights easily identified by the strong positive vertical gradients. Additionally, tropical instability can be seen as primarily originating from lower levels through increased warming and greater vertical instability.

As explained by Holton 1992, the vertical gradient of  $\theta_e^*$  can reveal the potential stability of the atmosphere where

$$\frac{d\theta_e^*}{dz} \left\{ \begin{array}{lll} < 0 & \text{conditionally unstable} \\ = 0 & \text{saturated neutral} \\ > 0 & \text{conditionally stable} \end{array} \right\} \quad (4.1)$$

A time cross section of  $\theta_e^*$  at *Kexue 1* in the southern SCS at 6N 110E (Fig. 4.7) during IOP1 reveals conditional instability primarily below 700 mb and near neutral stability up to the tropopause, approximately 100 mb, until about 15 May.

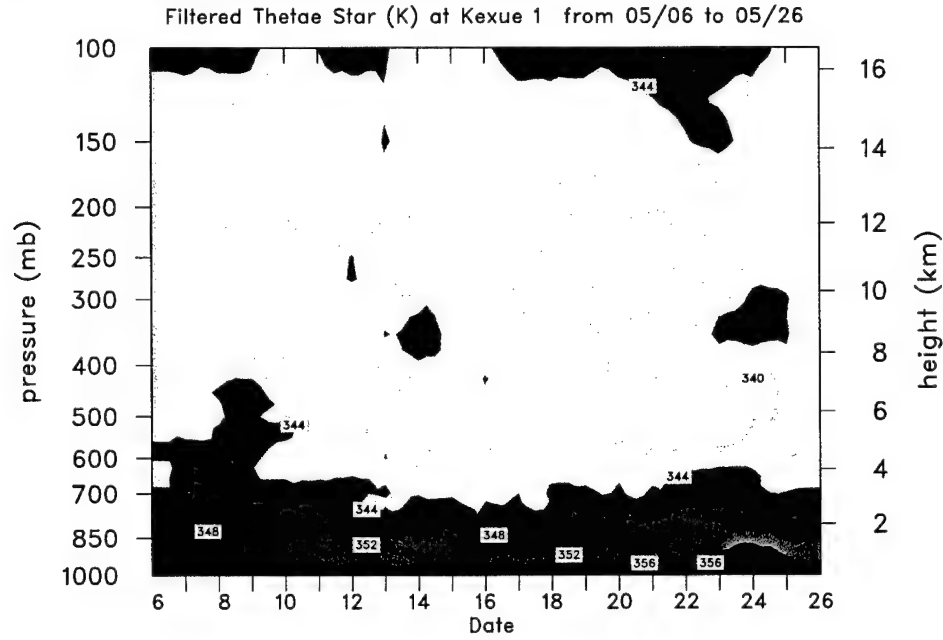


Figure 4.7: Time series of  $\theta_e^*$  at *Kexue 1* during IOP1

Conditional instability exists on 20 May from the surface to 500 mb, and extends to approximately 450 mb by 25 May. The initial onset of the 1998 monsoon in the southern SCS was

identified as 20-25 May by Lau, et al. (1999), 21 May by Li and Wu (1999), and 25 May by Chan et al. (2000). The increase of conditional instability agrees well with the timing of the onset noted by the authors above. Dips in the tropopause on 17 and 22 May and 11 June (Fig. 4.7) are not fully explained.

Farther north the  $\theta_e^*$  profile from the *Shiyan 3* (near 20N 117E, Fig. 3.1 for IOP1 (Fig.4.8) shows a lower tropopause than the *Kexue 1*. Using the 348 K contour as a marker for the tropopause height, trough-ridge couplets can be identified. Troughs can be readily seen on 7, 10, 15, and 17 May, which troughs match well with trough passages indicated by 500 mb streamlines and OLR (Figs. 4.9-4.12). In the  $\theta_e^*$  vertical profile, a peak in low-level warming occurs on 14 May. Figure 4.13 also shows a significant moisture increase also starting around 14 May. The low-level warming and increased moisture, along with the upper-level instability, show that two sources of instability, combined with an increased supply of moisture contributed to the northern SCS monsoon onset on 15 May (Johnson and Ciesielski, 1998).

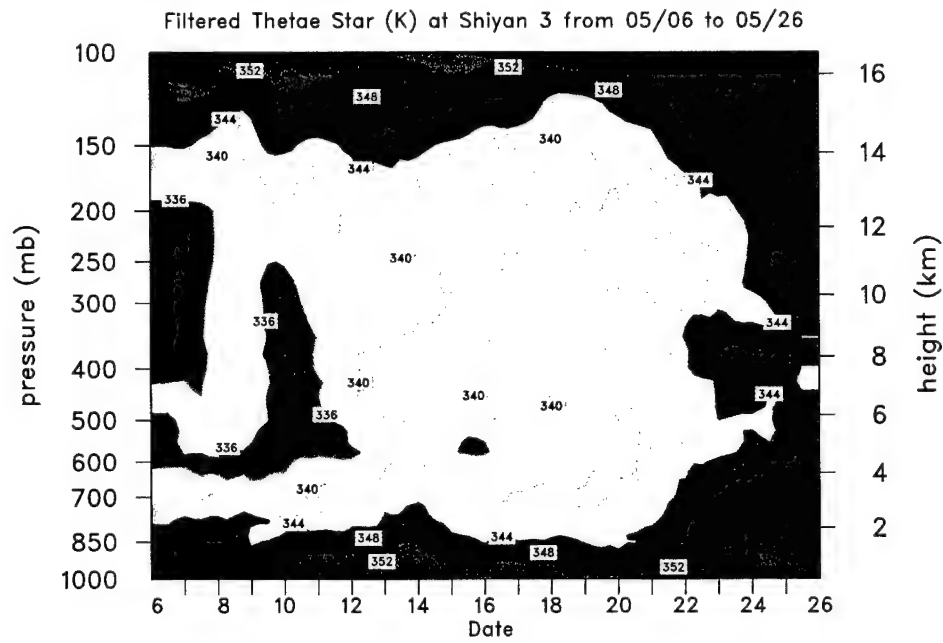


Figure 4.8: Time series of  $\theta_e^*$  at *Shiyan 3* during IOP1

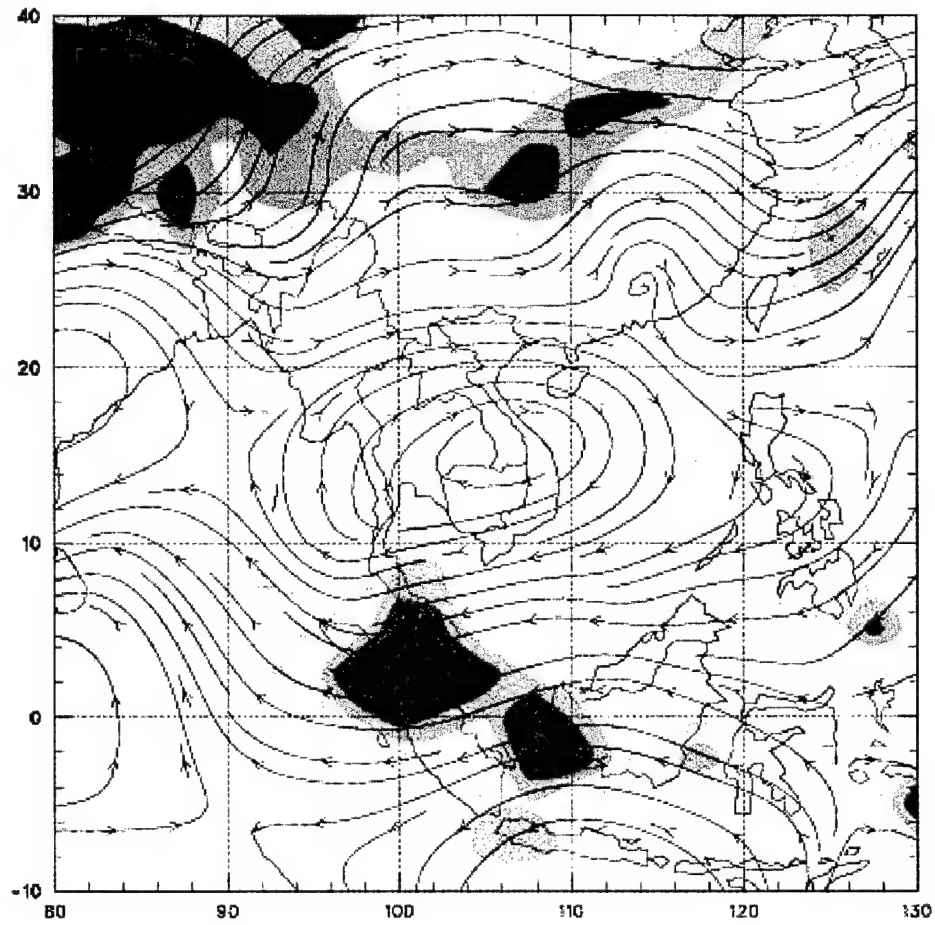


Figure 4.9: 500 mb streamlines and OLR for 7 May 1998 over the SE Asia region

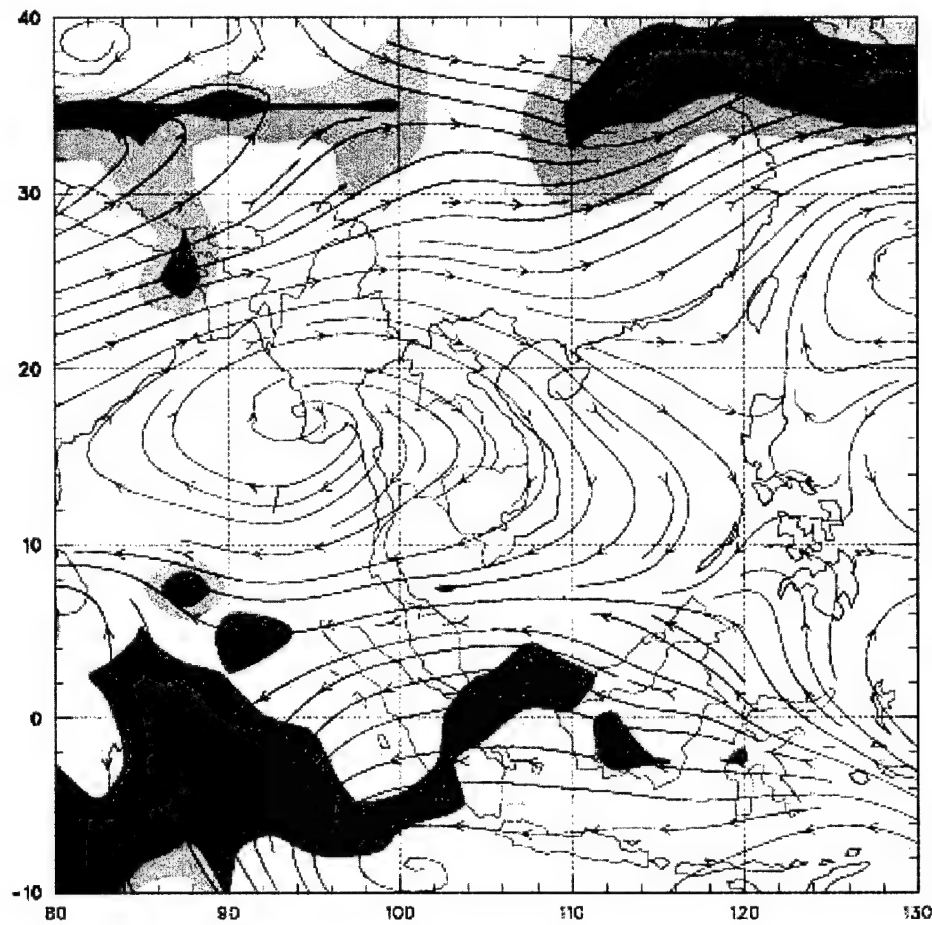


Figure 4.10: 500 mb streamlines and OLR for 10 May 1998 over the SE Asia region

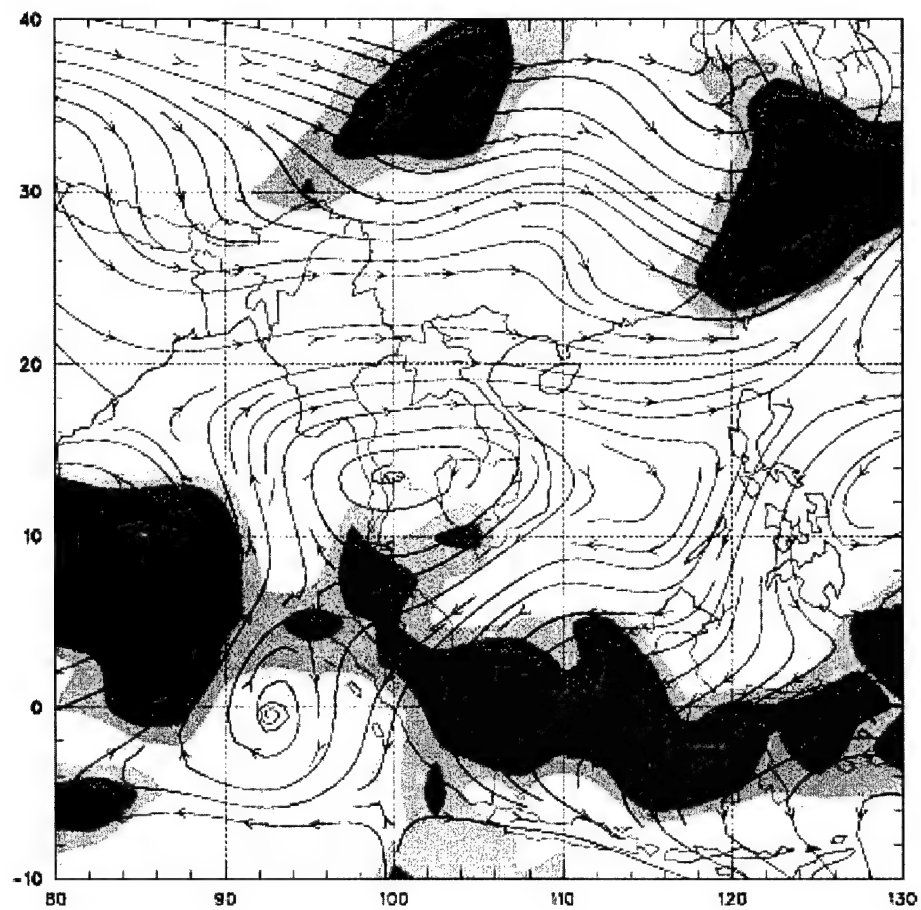


Figure 4.11: 500 mb streamlines and OLR for 15 May 1998 over the SE Asia region

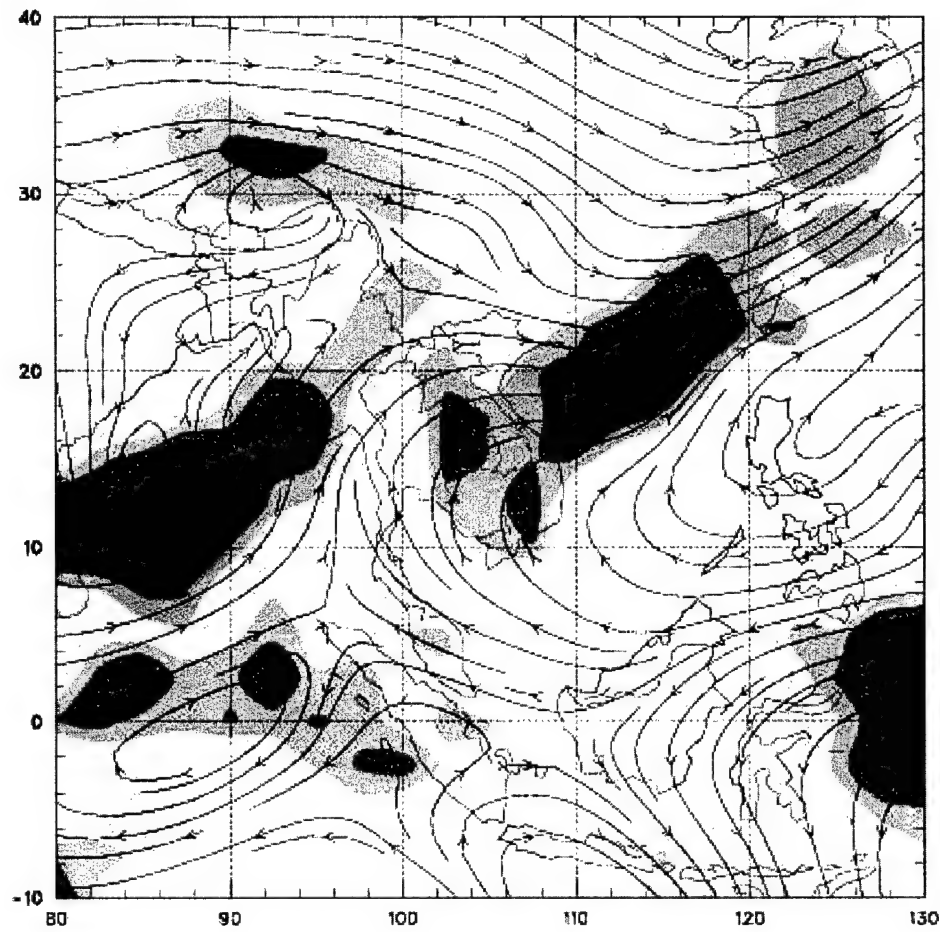


Figure 4.12: 500 mb streamlines and OLR for 17 May 1998 over the SE Asia region

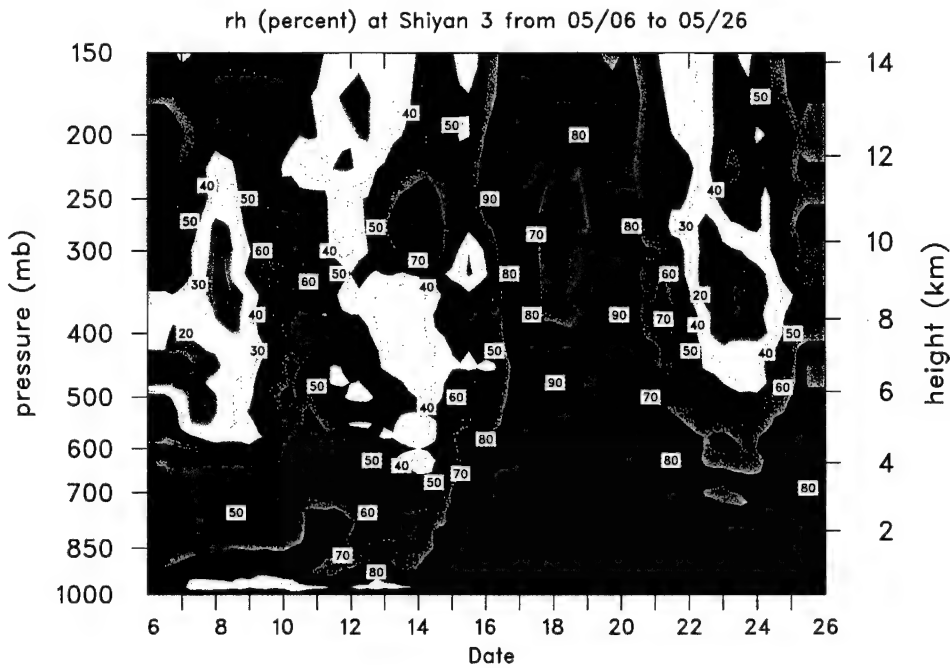


Figure 4.13: Time series of relative humidity at *Shiyian 3 during IOP1*

Li and Wu (1999) demonstrated with satellite analyses, precipitation analyses, and wind analyses that the increased rainfall over southern China that began on 15 May and progressed southward had significant midlatitude influences. Figure 4.14 clearly shows that the progression of precipitation is from north to south in mid-May. Figures 4.8, 4.11, 4.12, 4.14, 4.15–4.17 also support the assumption that the instability prior to 20 May was influenced by midlatitude influences. They show dips in the tropopause, cool pockets at mid- to upper-levels, and midlatitude troughs evident on streamline analyses.

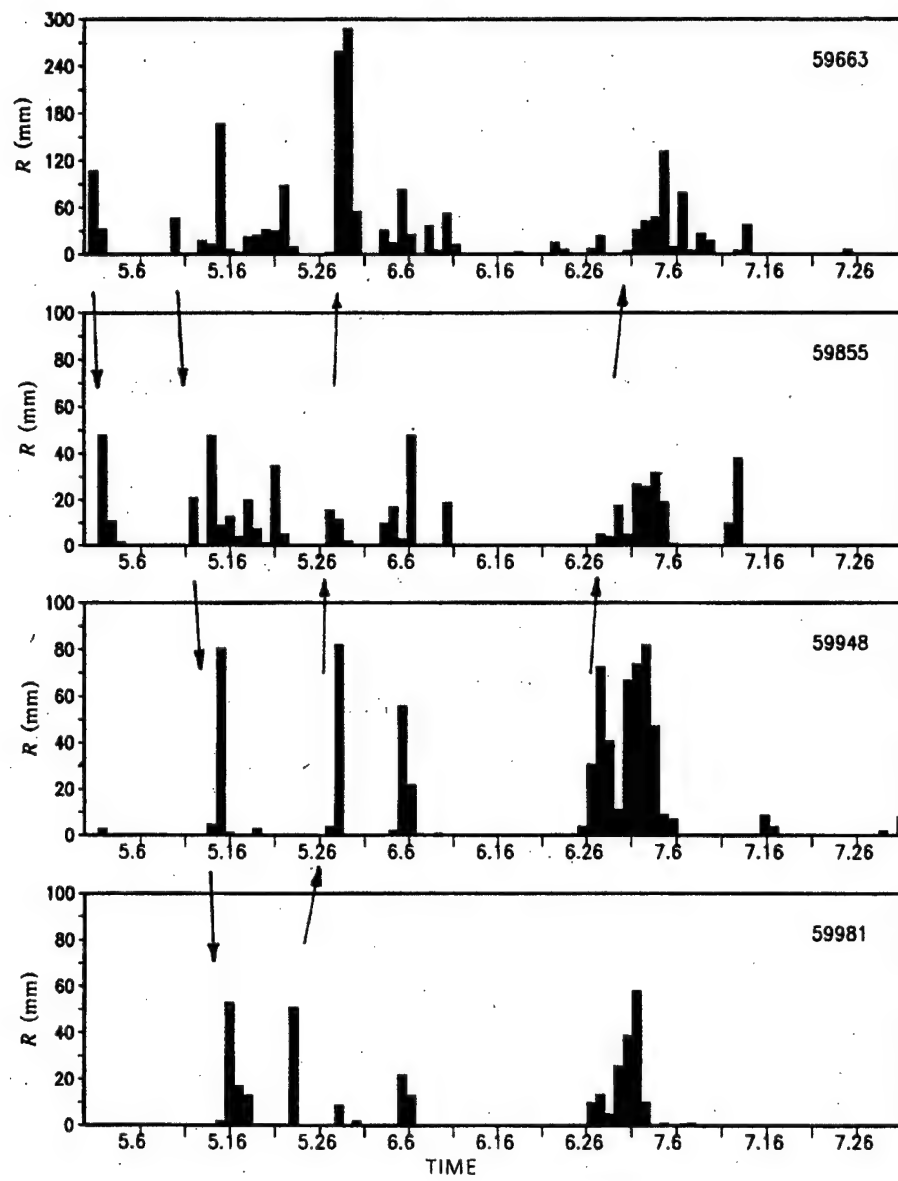


Figure 4.14: Daily precipitation at 4 stations during May 1–July 31, 1998. Stations are aligned from north to south, top to bottom, respectively. (Li and Wu, 1999)

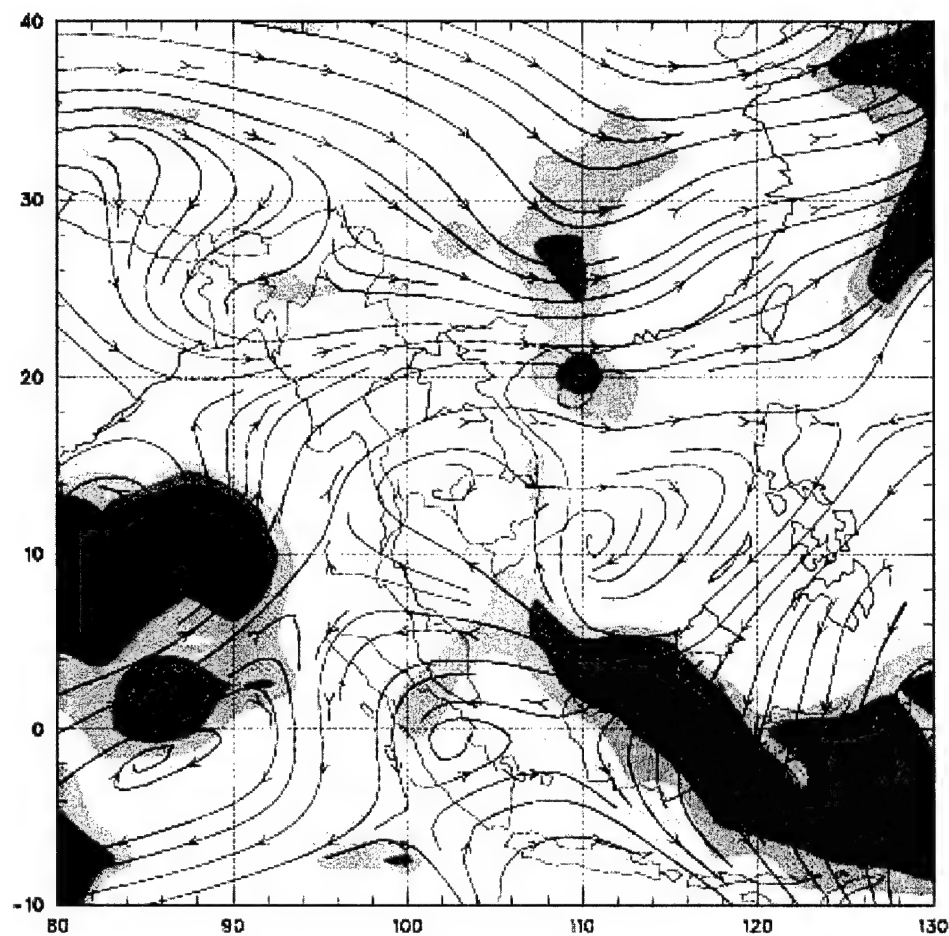


Figure 4.15: 500 mb streamlines and OLR for 16 May 1998 over the SE Asia region

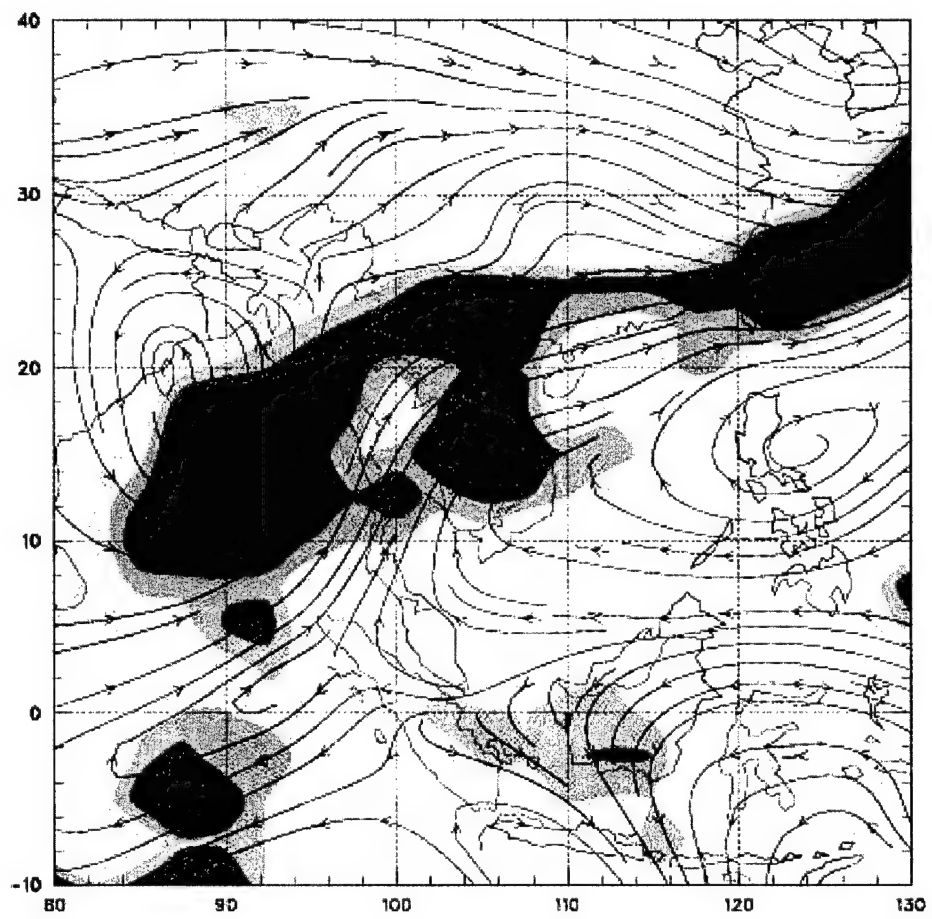


Figure 4.16: 500 mb streamlines and OLR for 18 May 1998 over the SE Asia region

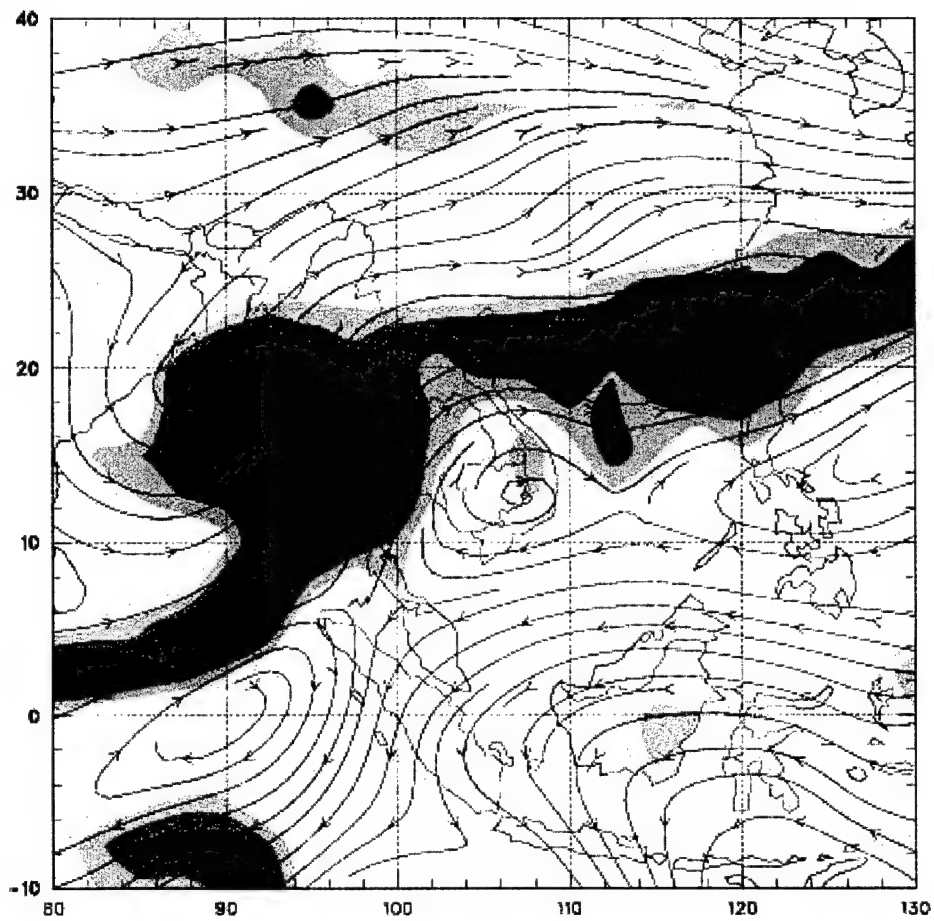


Figure 4.17: 500 mb streamlines and OLR for 19 May 1998 over the SE Asia region

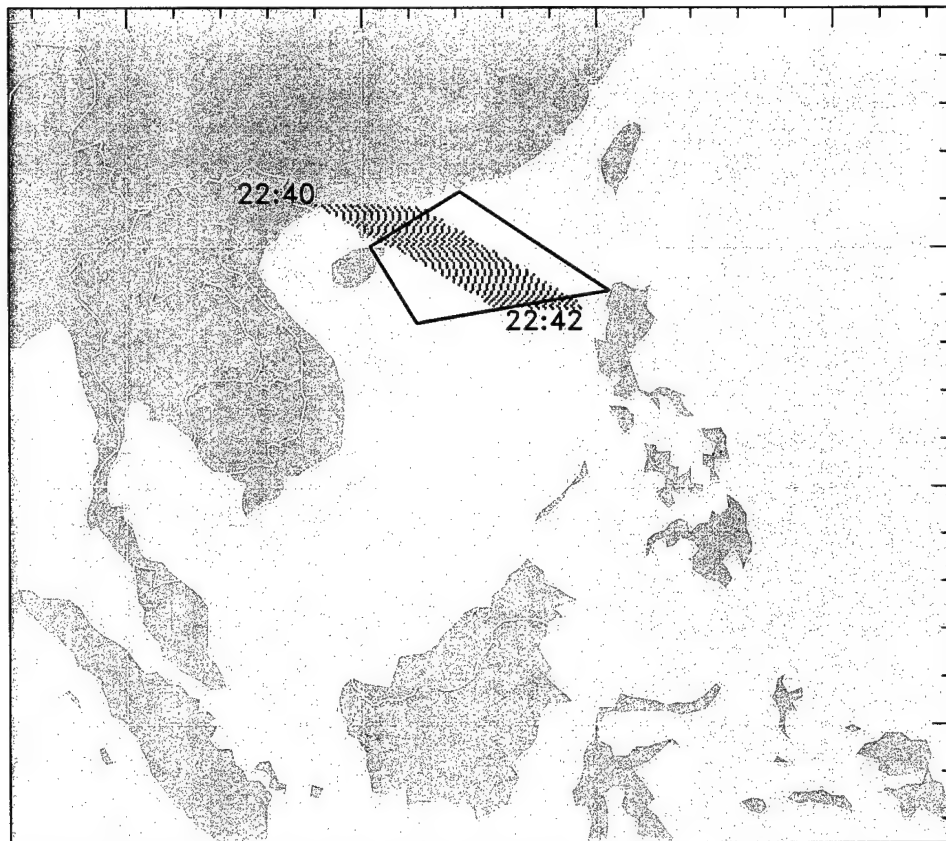
## **4.2 Precipitation Measurements**

In this section comparisons of standard rainfall estimations, derived from sounding data, are compared with independent sources such as the TRMM G2B31 combined rainfall estimates and the 3G68 TMI/PR rainfall estimates (Kummerow et al. 2000). On short time scales, rainfall estimates using the  $Q_2$  line integration technique are compared against the TRMM combined data. This is done by comparing data from a single TRMM satellite pass to polygons defined by four to five synoptic sounding sites. On longer time scales, pentad and two months, the moisture budget estimates are compared to the TRMM TMI and PR G3B68 data. As will be seen, the shorter time scales lead to little agreement between the two independent rainfall estimates while longer time scales using the budget estimates and TRMM data were more successful in reaching agreement between the two estimates.

### *4.2.1 $Q_2$ Line Integration Rainfall Estimates Compared to TRMM Combined TMI/PR Estimates*

The previous section identified periods that contained active convection and unstable stratification. Within these periods satellite imagery have been used to isolate active events in order to compare precipitation estimates from the line integration technique and TRMM combined data. Once active periods were identified, TRMM overpasses were matched to polygons defined by synoptic sounding sites. Within these polygons, the line integration technique was compared to the TRMM combined TMI and PR rainfall rates from the 2B31 algorithm. As noted from the example in Fig. 4.18 the areas of the polygons and TRMM overpasses are not identically matched. Additionally, the observation times of soundings and overpasses cannot be matched exactly due to the variable nature of the TRMM platform's orbit. The time difference between the TRMM overpasses and the soundings were 0.5-1.5 hours for the first three examples, orbits 2669, 2745, and 2997. Orbit 3043 had the greatest time differential at 3.5 hours.

TRMM overpasses on 06/05



TRMM Precipitation  
0.44mm/hr

Budget P-E  
0.43 mm/hr

Budget P  
0.64 mm/hr

Orbit #2997 0605 22:40-22:42UTC  
Sounding Time 060600 UTC

Figure 4.18: Example of TRMM orbit swath and bounding polygon used in line integration. The hatched swath indicates the area covered by TRMM and start and end times, UTC. Note the approximate time difference of 1.3 hour delay between swath start and end times and sounding time.

Table 4.1: Rainfall estimates from TRMM combined rainfall estimates and sounding derived line integration rainfall estimates.

Date/ Time	Orbit #	TRMM Rain mm/hr	Budget P-E mm/hr	E mm/hr	Budget P mm/hr	Area TRMM $10^5 \text{ km}^2$	Area Budget $10^5 \text{ km}^2$
0518/00Z	2699	0.27	0.61	0.16	0.77	2.16	1.65
0521/00Z	2745	1.06	1.22	0.15	1.37	2.49	2.43
0606/00Z	2997	0.44	0.43	0.21	0.64	2.47	3.56
0609/00Z	3043	1.46	2.22	0.24	2.46	0.67	1.99

The results given in Table 4.1 show little agreement using this technique on such a short time scale. Additional matching active rain events, sounding times and TRMM overpasses proved challenging and yielded few worthwhile examples. Therefore, this technique was replaced with comparing moisture budget rainfall estimates and TRMM data averaged over longer periods of time, as explained in the following sections.

#### 4.2.2 *Monthly averaged, and Diurnally Computed NESA Precipitation Estimates*

The lack of agreement between the rainfall estimates examined in the prior section led to examining data averaged over longer periods. Precipitation estimates from TMI, PR, and moisture budgets are compared on a diurnal time scale averaged for May and June.

Table 4.2 shows the NESA daily averaged rainfall estimates for TRMM and moisture budgets. The moisture budget estimates agree well with the PR data in May and with the TMI data in June. Figure 4.19 shows the average rainfall estimates over the NESA. The TRMM 3B42 rainfall estimates incorporate the TMI, TMI-PR combined data and Geostationary-IR observations as described in Kummerow et al. (2000). As seen by comparing Table 4.2 and Fig. 4.19, the moisture budget estimates are less than TRMM estimates in May and more than TRMM estimates in June.

Table 4.2: Rainfall estimates from TRMM TMI and PR algorithms and sounding derived moisture budgets, (MB)

Month	TMI mm/day	PR mm/day	MB mm/day
May	8.4	5.7	5.5
June	9.6	5.76	10.6

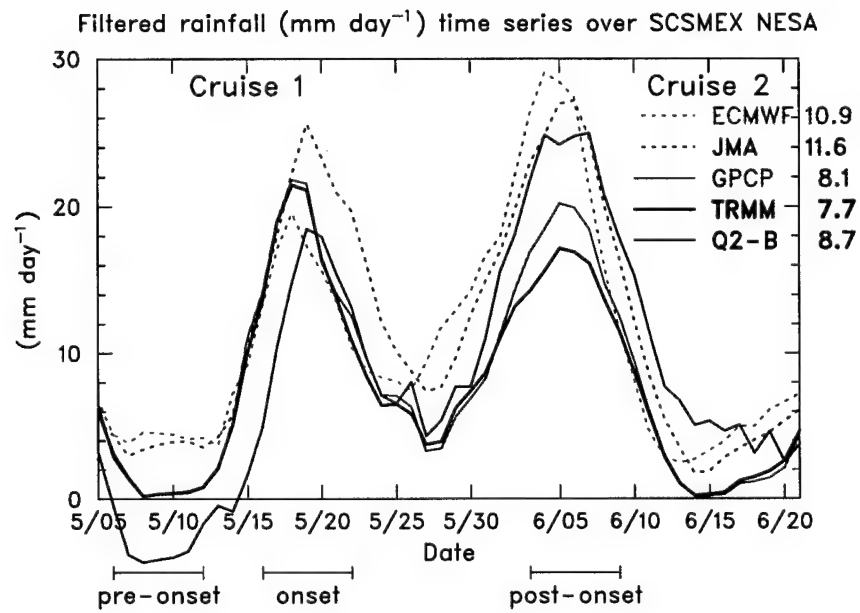


Figure 4.19: Rain rate estimates for NESA region from European Centre for Medium-Range Weather Forecasting (ECMWF), Japan Meteorological Agency (JMA), Global Precipitation Climatological Project (GPCP), TRMM-3B42, and Q2-B  $Q_2$  moisture budget precipitation estimates. Numbers to the right indicate total rainfall average estimates in mm/day.

As described in Chapter 3, rain rate measurements were binned into four different time intervals centered on 00, 06, 12, 18 UTC. The SCSMEX domain local time is UTC + 7 hours and the NESA local time is UTC + 8 hours. The TRMM data was from the 3G68 data set for the TMI and PR

Figures 4.20 and 4.21 show the diurnal cycle of rainfall for May and June in the NESA. In May and June all three estimates have similar profiles with maxima at 0800 LST and minima at 2000 LST.

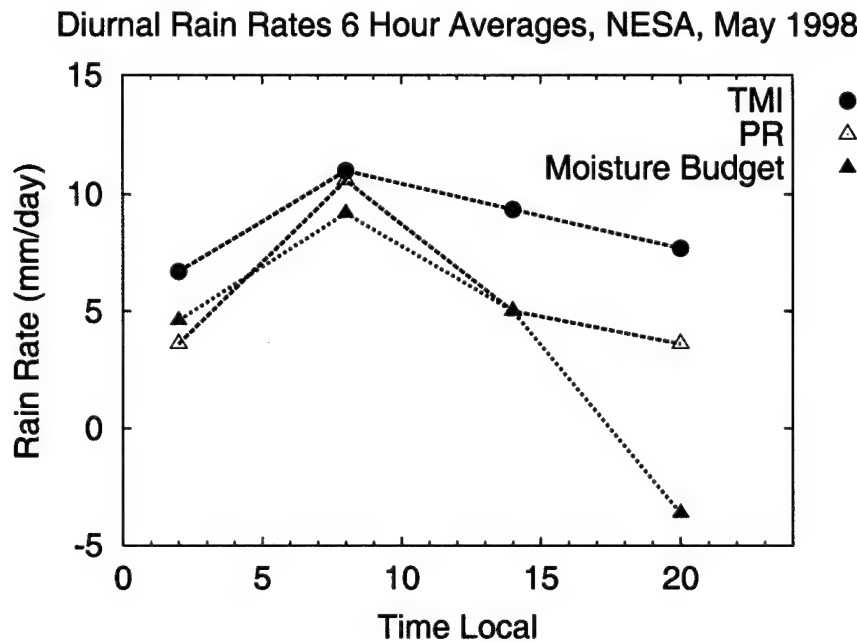


Figure 4.20: May rain rates for TMI, PR, and moisture budgets from the NESA region

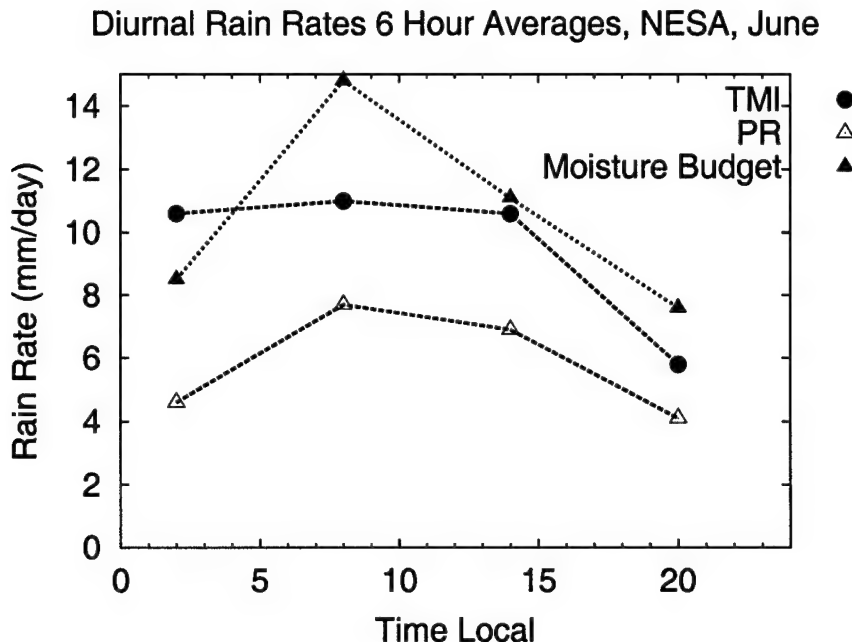


Figure 4.21: June rain rates for TMI, PR, and moisture budgets from the NESA

TRMM and moisture budget estimates for the NESA region, on a six-hour time scale, display a diurnal signal with a mid-morning peak. This peak, which is robust in all the data, is consistent with the diurnal cycle described by Gray and Jacobson (1977) for the open ocean. Dai (2001) summarized several studies using satellite data to confirm the existence of a morning maximum in oceanic convection and rainfall. Dai and Deser (1999) also revealed that maximum surface convergence occurs around 0600 LST in oceanic areas near continents.

Figures. 4.22 and 4.23 show that the moisture transport into the NESA is primarily zonal in origin. The meridional flow, from south to north, removes moisture from the NESA. This is easily seen by adding two moisture vectors north and south, or east and west. Therefore, over these two periods, we can say that the rainfall estimates computed over the NESA converge moisture primarily from the zonal flow. However, the diurnal variation in the total moisture convergence is influenced by diurnal changes in both zonal and meridional transports.

These figures also demonstrate that moisture storage and precipitation are oppositely re-

lated. The 0000 UTC (0800 LST) panels show precipitation to be a maximum and moisture storage to be a minimum. The 1200 UTC (2000 LST) panels show precipitation to be a minimum and the moisture storage to be a maximum. This pattern can be explained by precipitation which removes water vapor from the atmosphere, or the lack of precipitation, which allows water vapor to increase.

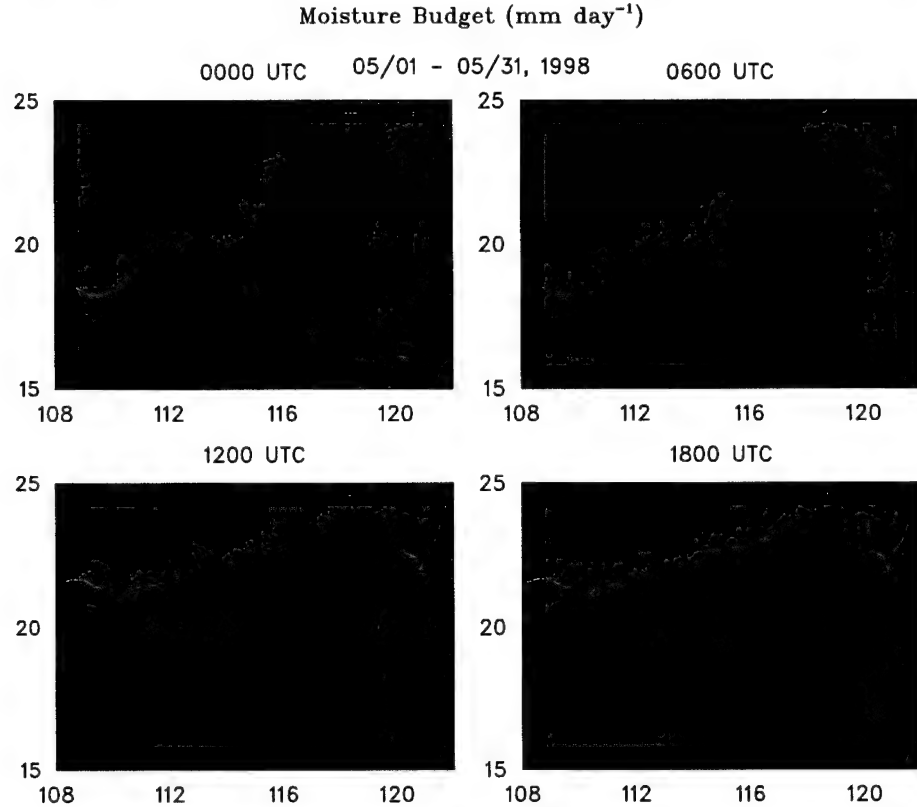


Figure 4.22: Moisture budgets with storage terms ( $dq/dt$ ), moisture convergence (MC), evaporation ( $E_o$ ), and precipitation ( $P_o$ ), May 1998, NESA. 0000 UTC = 0800 LST, etc.

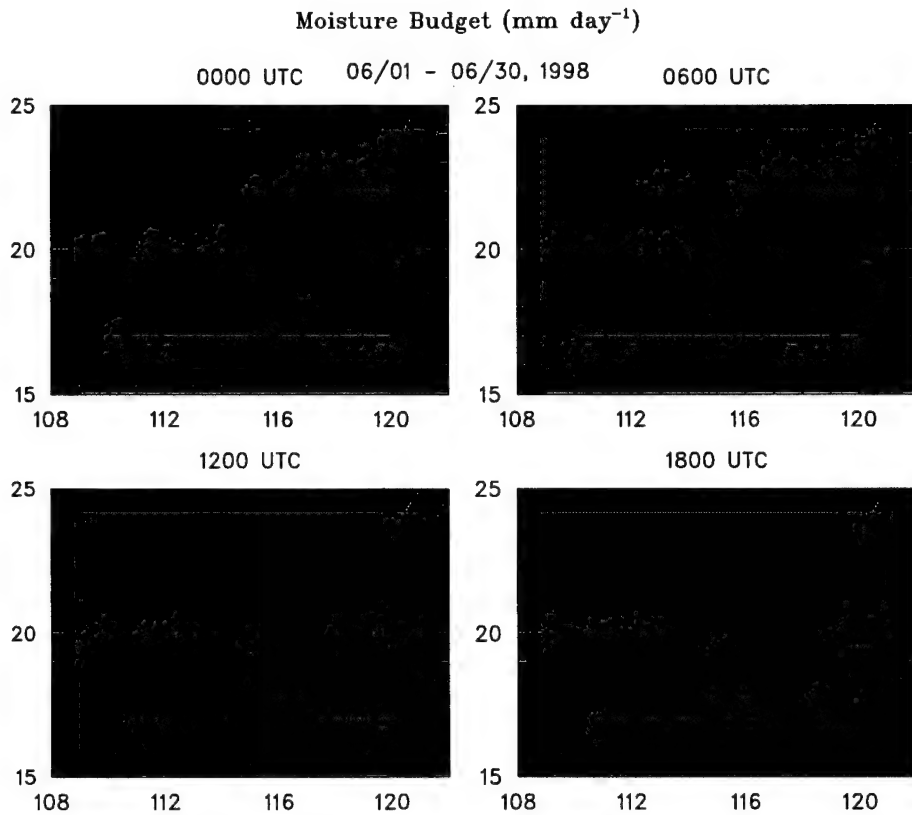


Figure 4.23: Moisture budgets with storage terms ( $dq/dt$ ), moisture convergence (MC), evaporation ( $E_o$ ), and precipitation ( $P_o$ ), June 1998, NESA. 0000 UTC = 0800 LST, etc.

To help clarify the diurnal moisture transport process, the second onset period, 1–10 June, is examined. This second onset period is shown in Fig. 4.19. Figure 4.24 displays the diurnal divergence fields during the second onset period. In general, low-level convergence is associated with convection. The areas of offshore convergence are clearly seen at 0800 LST and 0200 LST. Areas of onshore convergence are noted at 1400 LST and 2000 LST. These patterns are consistent with land and sea breeze effects.

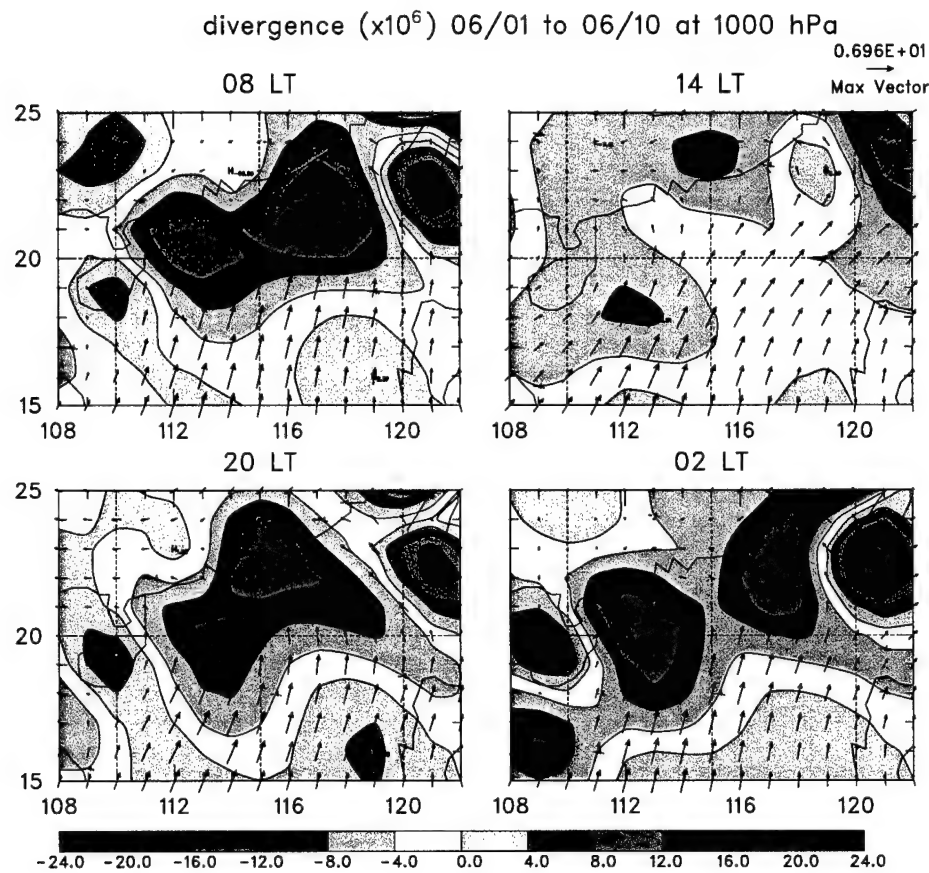


Figure 4.24: Divergence fields over NESAs for 1-10 June 1998. Arrows indicate wind field.

To further explore the diurnal cycle, a wind rose of the 850 mb winds for Hong Kong is plotted in Fig. 4.25 for the period 1-10 June. An inertial oscillation was also noted for the initial onset period, 15-25 May, but at a reduced amplitude. These oscillations are similar to those associated with nocturnal low-level jets (LLJs) in the midwestern United States documented by Whiteman (1997), but the tropical oscillations lack the strength of these LLJs. Structural differences in the two oscillations are noted by examining Whiteman's oscillation in Fig. 4.26a. In particular, the strongest flow over the Great Plains occurs from 2000 LST. The weakest southerly flow at Hong Kong is at 2000 LST. These differences can be explained by considering the vertical circulation in land and sea breezes along the southern China coast. During the afternoon, there is a sea breeze,

but the return flow aloft, typically near 1.5 km (Banta 1995), produces a northerly component at 850 mb - so it reduces the southerly flow at 1400 LST and 2000 LST (Fig. 4.25). At night, the return flow aloft from the land breeze enhances the southerly flow at 0200 LST and 0800 LST.

### Hong Kong

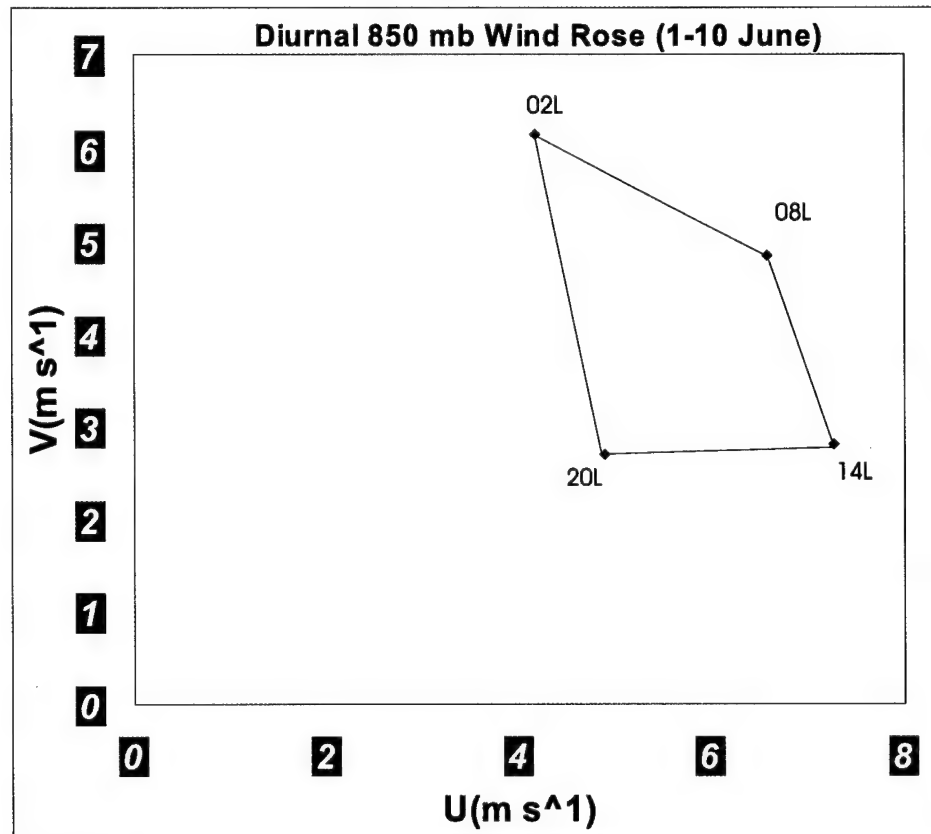


Figure 4.25: Hong Kong wind rose at 850 mb, averaged from 1-10 June.

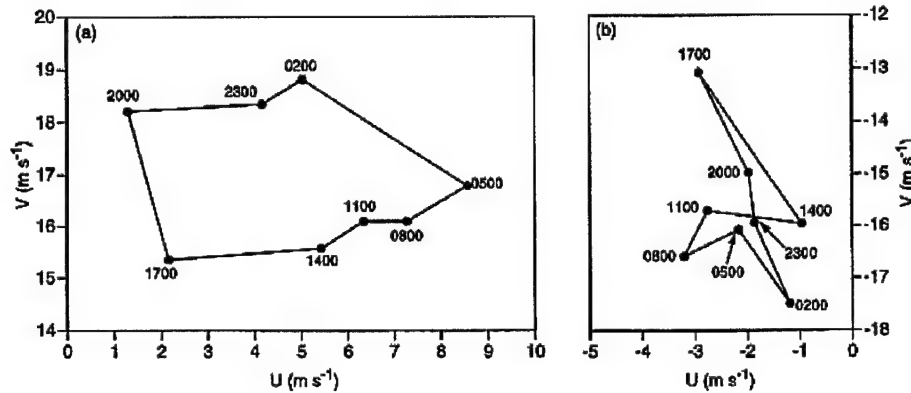


Figure 4.26: Diurnal oscillations of wind speed and direction at the maximum jet wind level for (a) southerly and (b) northerly LLJs. The U represents the eastward wind speed component and V the northward component. Indicated times are central standard time. Data collected over a two year period. (Whiteman et al. 1997)

#### 4.2.3 Two-Month averaged, and Diurnally Computed SCSMEX and NESA Precipitation Estimates

The previous section demonstrated that a clear 0800 LST maximum and a 2000 LST minimum existed in precipitation estimates when averaged over one month. Over a longer time scale of two months, the TRMM and moisture budget data are now used to determine the diurnal cycle of precipitation over the larger SCSMEX and the NESA region.

The composite (Fig. 4.27) compares the TRMM data, moisture budget data, and Dongsha Island rain gauge data over the NESA. The mid morning peak is again prevalent in each estimate. Although the number of rainfall events for the gauge data ranges from eight to fifteen events per bin, it matches well with the overall pattern of the other three estimates. The moisture budget data falls roughly between the TMI and PR data when averaged over the two month period. The consistency between these independent rainfall estimates suggests that they provide an accurate portrayal of the

diurnal signal on this time scale.

The two-month rainfall estimate average over the SCSMEX region shown in, Fig. 4.28, reveals a mid-morning maximum and an early morning minimum. The early morning minimum may reflect that the SCSMEX region contains more land surface than the NESA which contains primarily an ocean surface. The amplitude for the SCSMEX region is less than that for the NESA, indicating that NESA region may have received more rainfall during May-June 1998 than the larger SCSMEX region on average.

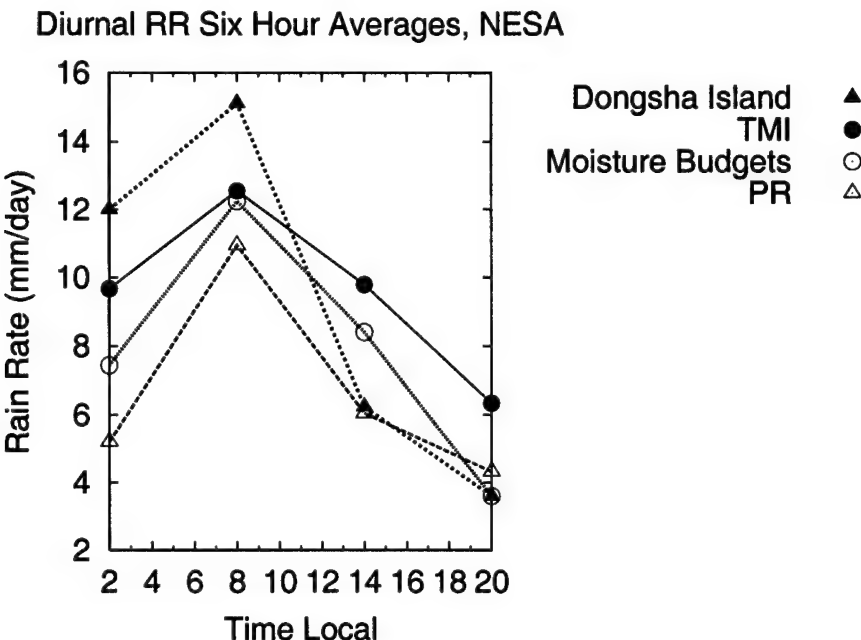


Figure 4.27: Rain rates in the NESA region for May and June 1998.

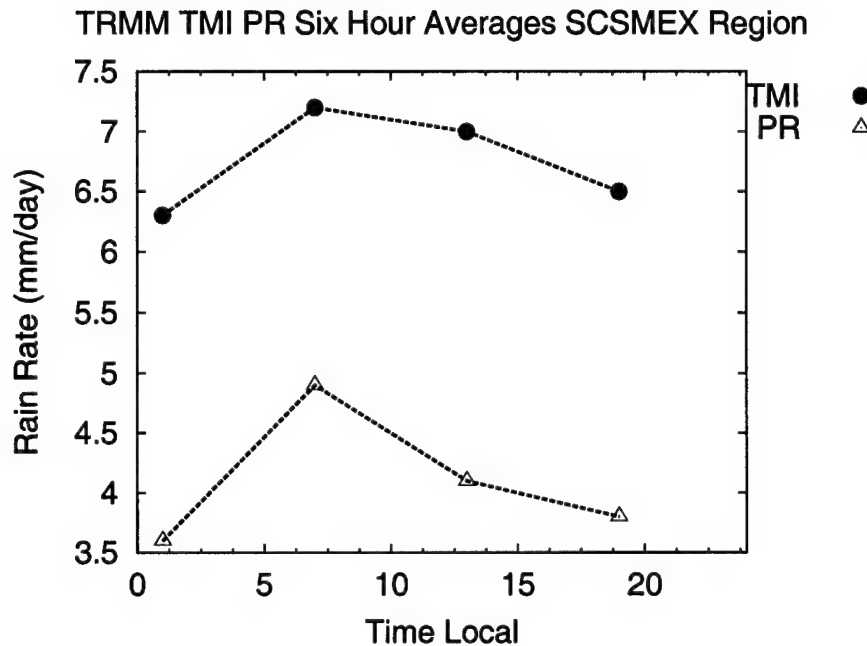


Figure 4.28: TMI and PR rain rates in the SCSMEX region for May and June 1998.

When the TMI and PR data were examined using three-hour intervals, a semidiurnal signal is present over the NESAs as seen in Fig. 4.29. This semidiurnal signal was also noted in the SCSMEX region, but only in the TMI data (Fig. 4.30). Schumacher and Houze (2000) found a similar semidiurnal cycle in PR data from 50 passes over the Kwajalein validation area for Aug 1998-Aug 1999. However, the PR data from Kwajalein bore little resemblance to the rain gauge data within the validation area. The gauge data for Dongsha Island during May and June 1998 contained only four to thirteen events per bin and are therefore not included in Fig. 4.29.

### TMI PR Diurnal Rain Rates 3 Hour Averages, NESA

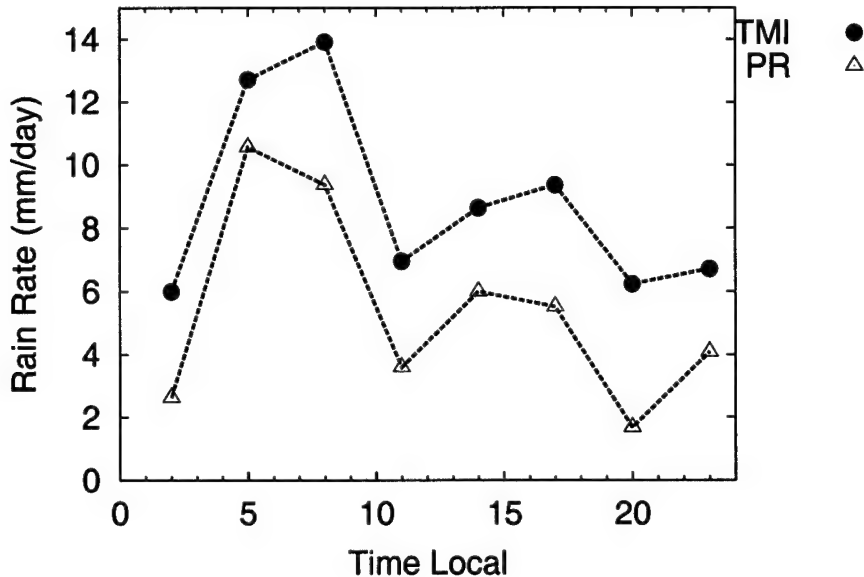


Figure 4.29: TMI and PR rain rates averaged in 3 hour intervals in the NESA region for May and June 1998.

As mentioned above, the semidiurnal signal is also evident in the TMI data over the SCSMEX region (Fig. 4.30). The mid-morning peaks occur at 0800 LST for both the PR and TMI as seen over the NESA. However the afternoon peak is only present in the TMI at 1600 LST. Reasons for the lack of a semidiurnal signal in the PR over the SCSMEX region are not clear: however, as Schumacher and Houze (2000) point out, sampling errors associated with the use of the PR data on monthly time scales limit the ability to detect the semidiurnal cycle with that data source.

TRMM PR Diurnal RR Three Hour Averages SCSMEX Region

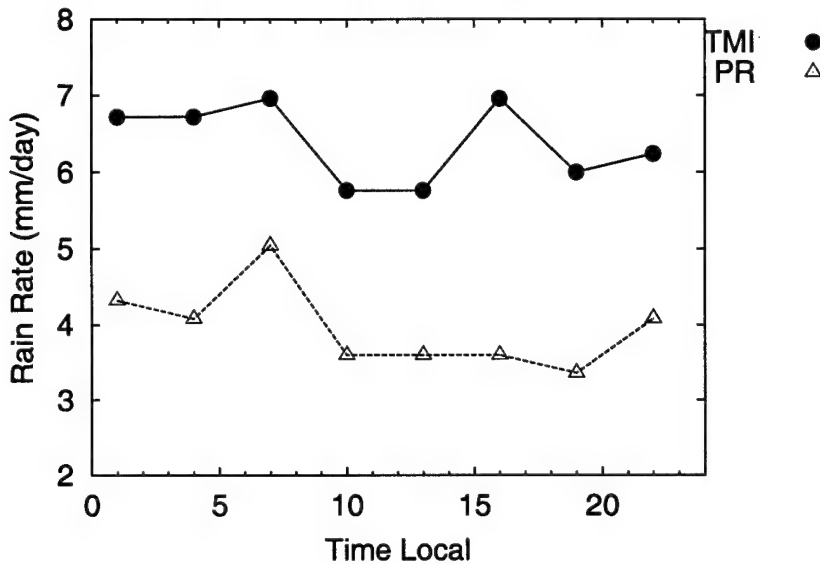


Figure 4.30: TMI and PR rain rates averaged in 3 hour intervals in the SCSMEX region for May and June 1998.

Figures 4.31, 4.32, 4.33, and 4.34 show the diurnal signal over the SCSMEX and NESA regions in relation to the variability (standard deviation) of the data at each time. Over the SCSMEX region (Figs. 4.31 and 4.32) the mid-morning peak contains the highest variability, suggesting that larger rainfall events take place in the window between 0400 LST and 1000 LST or centered on 0700 LST. The results for the NESA are not as clear. The highest variability for the TMI takes place at 0200 LST while the highest variability for the PR occurs at 0800 LST. Work by Lim and Suh (2000) (Fig. 4.35a) agree with the findings from the PR data over the NESA. They used assimilated data from the Goddard Earth Observing System (GEOS-1) to show that during the boreal summer, heaviest rainfall takes place near 0700 LST over the entire SCS. The semidiurnal signal shown in Fig. 4.36 shows that much of the land signals display peaks approximately near 1400 LST and 0200 LST. These results are harder to match to Fig. 4.30 due to the land and sea distribution over the SCSMEX region.

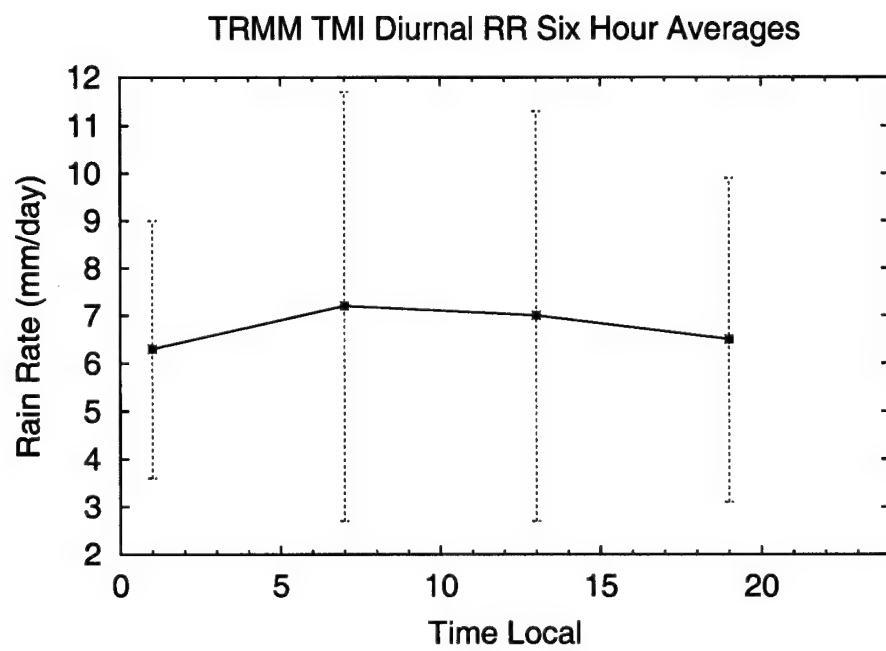


Figure 4.31: Diurnal variation in rain rates from TRMM TMI for the SCSMEX region during May and June 98. Error bars represent one standard deviation.

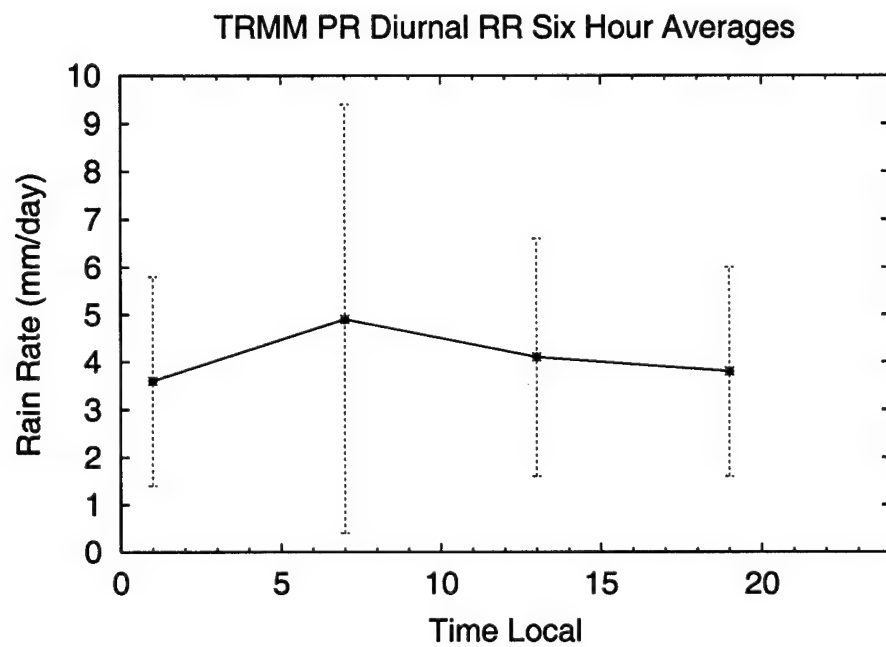


Figure 4.32: Diurnal variation in rain rates from TRMM PR for the SCSMEX region during May and June 98. Error bars represent one standard deviation.

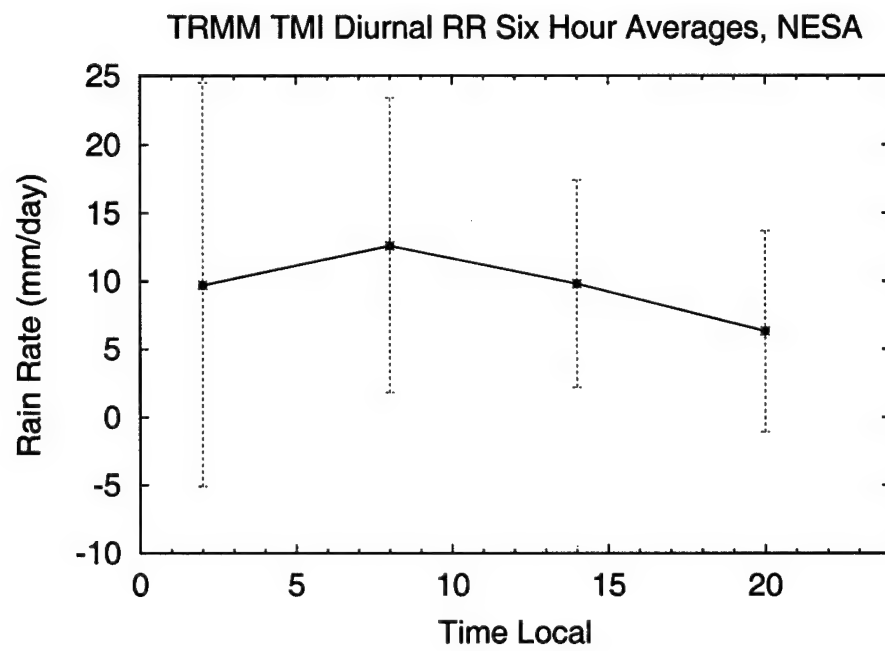


Figure 4.33: Diurnal variation in rain rates from TRMM TMI for the NESA region during May and June 98. Error bars represent one standard deviation.

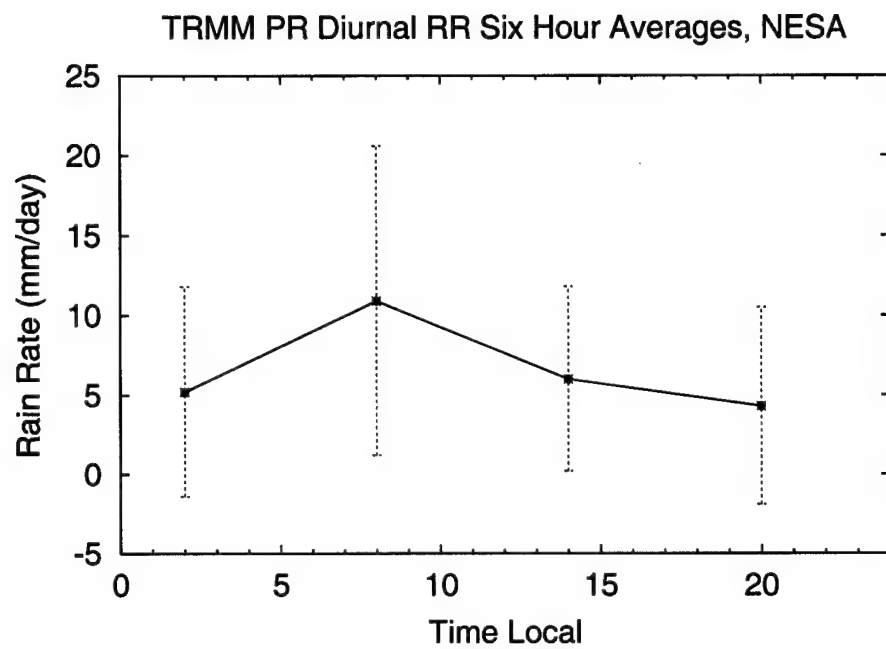


Figure 4.34: Diurnal variation in rain rates from TRMM PR for the NESA region during May and June 98. Error bars represent one standard deviation.

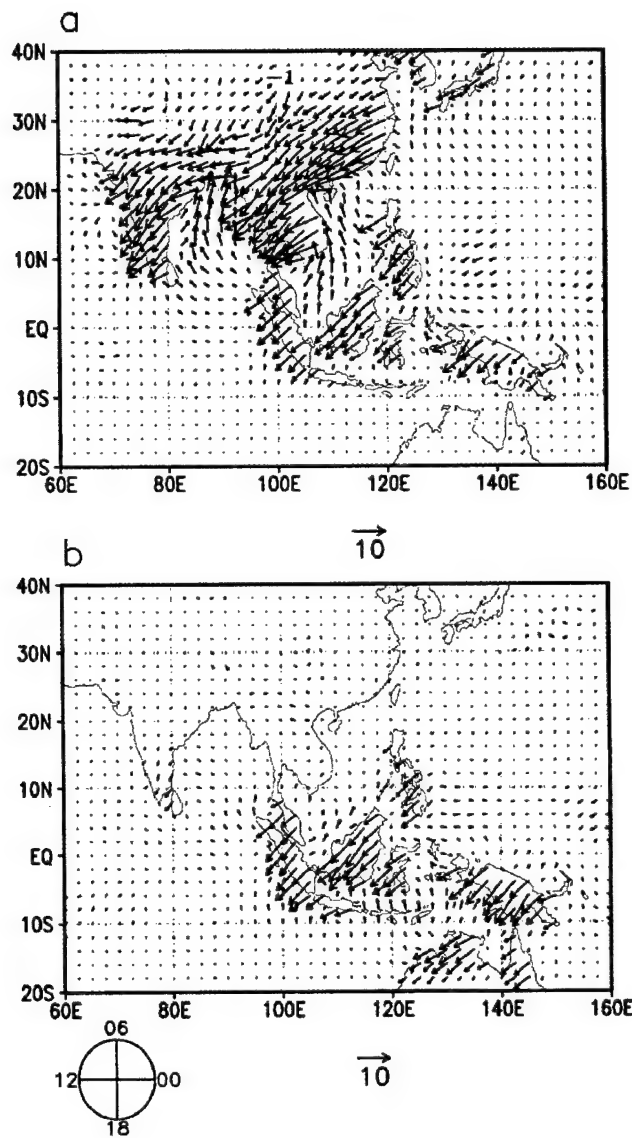


Figure 4.35: Harmonic dials of diurnal precipitation for the (a) boreal summer and (b) wintertime for the Maritime Continent. They were calculated by averaging the amplitudes and phase of harmonic dial in polar coordinates for each day of the entire data period. Peak time can be read in local solar time as marked in the diagram below the lower left of (b). The eastward arrow indicates the hour of maximum occurred at 0000 LST. Phase in hour increases counterclockwise. The scale for the arrows is given in  $\text{mm day}^{-1}$  below the bottom of each figure. The dials were drawn at every grid point to show detailed change of harmonic arrows in their magnitude and orientation. (Lim and Suh, 2000)

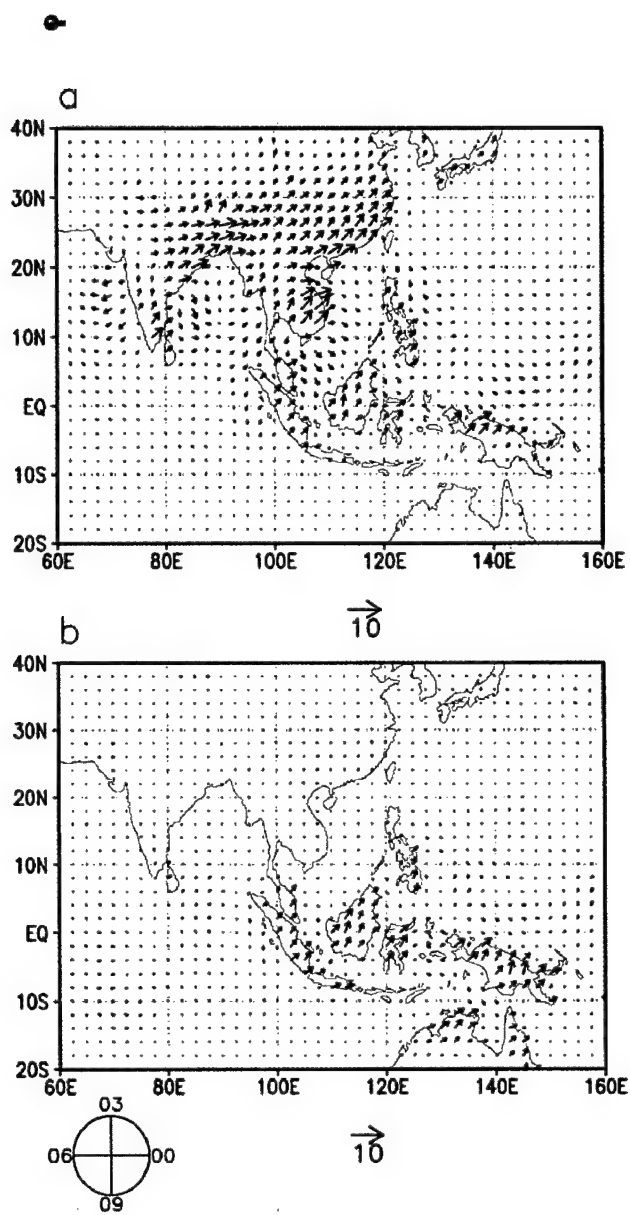


Figure 4.36: As in Fig. 4.35, except for the semidiurnal component of the assimilated amounts of precipitation. (Lim and Suh, 2000)

#### 4.2.4 Diurnal Cycle of Heavy Precipitation, NESA

In an attempt to examine the diurnal cycle of heavy precipitation, rain rates greater than 7.6 mm/hr in TRMM data were examined over the northern SCS for comparison with the oceanic environment examined by Gray and Jacobson (1977). Rain rates were binned in 6 hour intervals due to the reduced sample size over the NESA. The data set for Gray and Jacobson was much larger than the two month period examined in this study. Despite this difference, Fig. 4.37 suggests that a diurnal signal is present in the PR and combined rainfall estimates. The TMI data shows an afternoon peak, but due to the dissimilar footprints of the PR and TMI and the small sample size, caution must be exercised in drawing conclusions on the diurnal cycle from this example. Figure 4.37 displays some evidence that the diurnal signal for the NESA may be similar to the open-ocean heavy convection found earlier by Gray and Jacobson. However, further investigation is needed.

TMI PR Combined Diurnal Rain Rates > 7.6mm/hr, NESA

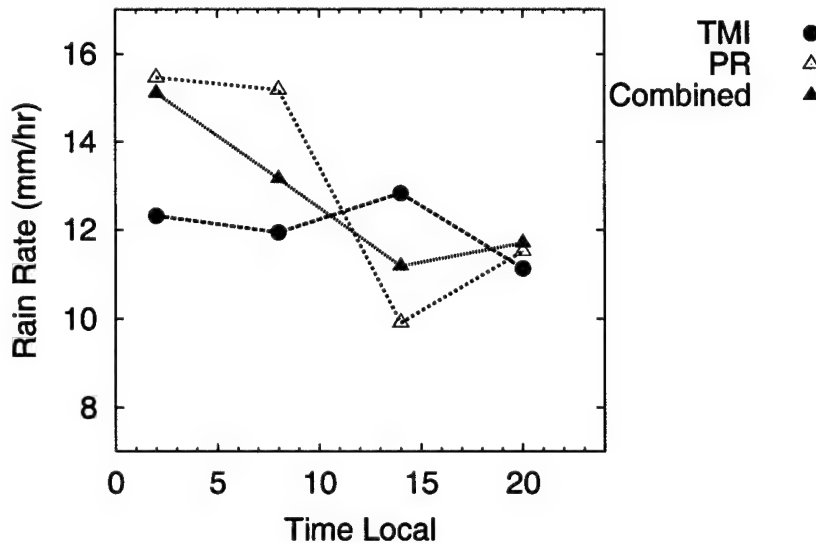


Figure 4.37: TMI, PR, and combined rain rates greater than 7.6 mm/hr over the NESA

## **Chapter 5**

### **CONCLUSIONS**

In this study, multiscale variability (seasonal to diurnal time scales) of the circulation and precipitation over the East Asian monsoon has been investigated using data from the May–June 1998 South China Sea Monsoon Experiment (SCSMEX). Streamline analysis clearly displays an onset vortex for the 1998 SCS monsoon. The importance of a vortex in the Arabian Sea for the onset of the Indian monsoon was described by Krishnamurti (1981). The vortex identified over the Bay of Bengal (BOB) served several purposes in setting the stage for the onset of the SCS monsoon. It replaced the low-level anticyclonic circulation over the BOB and helped shift the easterly trade winds over the region to a moist southwesterly monsoonal flow. The vortex also set up the upper-level circulation over the Indochina peninsula which finally migrated to the west, eventually becoming the Tibetan anticyclone.

Midlatitude influences and low-level warming were contributing factors for the convection starting on 15 May in the northern SCS. The low-level warming was accompanied by a significant period of high OLR and upper-level convergence during the pentad 11–15 May. Both factors indicate a cloud-free region and increased solar insolation to account for increase in the low-level temperature profile. Several midlevel troughs were found to occur shortly after the peak in low-level warming, providing evidence that two sources of instability contributed to the monsoon onset in the northern SCS. Tropical and mid-latitude influences, found in the 1998 SEAM, are typical of other onset patterns found in other years.

On all time and space scales analyzed in this study, a morning precipitation maximum was

present in rainfall estimates. However, to say that a morning maximum of precipitation exists at all points in the SCSMEX and NESA region is not true. On average, when analyzed on six-hour intervals, a midmorning maximum is consistent with TRMM and sounding-derived rainfall estimates. When analyzed over three-hour intervals, semidiurnal signals are noted over the NESA in the TMI and PR data. This bimodal distribution is also present in the TMI data over the larger SCSMEX region but not found in the PR rainfall estimates in this study.

The importance of accurately forecasting the onset of the SCS monsoon cannot be underestimated for the multitude living in this part of the world. Forecasters can use this study as a model case in which a vortex develops in the BOB and convection, in this case, started in the northern SCS three days later. The vortex should be accompanied by midlatitude troughs propagating off the southern coast of China. This is a classic example of the processes outlined by Loechl (2001).

### 5.0.5 *Future Work*

Accurate forecasting of the onset and strength of the SCS monsoon could literally mean life or death to many people in East Asia. One key factor in unlocking this mystery is understanding the interactions between the 30–60 day Madden–Julian Oscillation and the 12–24 day midlatitude oscillations (Loechl 2001). Timing of these two features may help in predicting onset dates of the SCS monsoon.

TRMM has the potential to help refine climatological tables for the diurnal cycle on a much higher resolution than ever before possible. Given large enough sample sizes, the diurnal cycle can be determined for smaller regions over the tropics. Ultimately each 4x4 km pixel in the TRMM data could have its own diurnal rainfall cycle. TRMM data can be easily partitioned over countries and regions of vital national interest.

Understanding the diurnal rainfall cycle on a monthly scale is very important to military planners and forecasters. Every operation in peace time and war has meteorological limits that commanders must observe in order for any given mission to be successful ensure protection of

aircraft and personnel. Long range planners determine the optimal time to start an operation by considering average meteorological conditions and the impact those conditions have on operations. The primary tool for forecasters in the tropics is climatology. Climatology provides the boundaries of a forecast, freeing the forecaster to use other tools to fine-tune his products for the critical hour. Currently diurnal tables are based upon sparse rain gauge networks throughout the tropics. Subjective interpolation between gauges is used to determine diurnal cycles for regions not covered by raingauge data.

TRMM data can provide planners and forecasters with objective estimates of the local diurnal cycle in areas without gauges.. These estimates capture the local effects that may escape a simple linear interpolation between gauges and possibly be the difference between a sucessful mission and a failure.

## **Chapter 6**

### **APPENDIX**

Table 6.1: List of abbreviations and symbols

---

<b>BOB</b>	Bay of Bengal
<b>DNS</b>	Day-vs-Night Subsidence
<b>ECMWF</b>	European Centre for Medium-Range Weather Forecasts
<b>EFOV</b>	Effective Field of View
<b>GAME</b>	GEWEX Asian Monsoon Experiment
<b>GEOS</b>	Goddard Earth Observing System
<b>GEWEX</b>	Global Energy and Water cycle Experiment
<b>IOP</b>	Intensive Observation Period
<b>LLJ</b>	Low Level Jet
<b>LST</b>	Local Standard Time
<b>MQD</b>	Multiquadratic
<b>NESA</b>	Northern Enhanced Sounding Array
<b>OLR</b>	Outgoing Longwave Radiation
<b>PR</b>	Precipitation Radar
<b>RFC</b>	Radiative Cloud Forcing
<b>SCS</b>	South China Sea
<b>SCSMEX</b>	South China Sea Monsoon Experiment
<b>SEAM</b>	Southeast Asian Monsoon
<b>TMI</b>	TRMM Microwave Imager
<b>TRMM</b>	Tropical Rainfall Measuring Mission
<b>TUTT</b>	Tropical Upper Tropospheric Trough
<b>UTC</b>	Universal Coordinate Time
<b>WPSR</b>	Western Pacific Subtropical Ridge
<b>c</b>	Condensation
<b>e</b>	Evaporation
<b>E</b>	Surface Evaporation
<b>L</b>	Latent Heat of Condensation
<b>p</b>	Pressure
<b>P</b>	Precipitation
<b>q</b>	Specific Humidity
<b><math>Q_2</math></b>	The Apparent Moisture Sink
<b><math>\langle Q_2 \rangle</math></b>	Vertically Integrated $Q_2$
<b>t</b>	time
<b>v</b>	Wind Vector
<b><math>\theta_e^*</math></b>	Saturated Equivalent Potential Temperature
<b><math>\omega</math></b>	Vertical Pressure Velocity

---

## Chapter 7

### REFERENCES

- Asai, T., S. Ke., and Y. Kodama, 1999: Diurnal variability of cloudiness over East Asia and the western Pacific Ocean as revealed by GMS during the warm season. *J. Met. Soc. Japan*, **76**, 675–684.
- Barnes, S. L., 1964: A technique for maximizing details in numerical weather map analysis. *J. App. Met.* **3**, 396–409.
- Betts, A. K., et al., 1994: Relation between mean boundary layer structure and cloudiness at the R/V valdivia during ASTEX. *J. Atmos. Sci.*, **52**, 2752–2762.
- Chan, J.C.L., Y. Wang, and J. Xu, 2000: Dynamic and thermodynamic characteristics associated with the onset of the 1998 South China Sea monsoon. *J. Met. Soc. Japan*, **78**, 367–380.
- Chang, C.-P., George T.-J. Chen, 1995: Tropical circulations associated with southwest monsoon onset and westerly surges over the South China Sea. *Mon. Wea. Rev.*, **123**, 3254–3267.
- Chen, T.-C., et al. 1999: Diurnal and seasonal variations of the rainfall measured by the automatic rainfall and meteorological telemetry system in Taiwan. *Bull. Amer. Meteor. Soc.*, **80**, 2299–2312.
- Chen, T.-C., and J.-M. Chen, 1995: An observational study of the South China Sea monsoon during the 1979 Summer: Onset and life cycle. *Mon. Wea. Rev.*, **123**, 2295–2318.
- Chen, S. S., R. Houze Jr., B. E. Mapes, 1996: Multiscale variability of deep convection in relation to large-scale circulation in TOGA COARE. *J. Atmos. Sci.*, **53**, 1380–1409.

- Cole, H., 1993: The TOGA-COARE ISS Radiosonde temperature and humidity sensor errors. NCAR Tech. Rep. SSSF, 26 pp.
- Cressman, G. P., 1959: An operational objective analysis scheme. *Mon. Wea. Rev.*, **87**, 367–374.
- Dai, A., 2001: Global precipitation and thunderstorm frequencies. Part II: Diurnal variations. *J. Climate*, **14**, 1112–1128.
- Dai, A., and C. Deser, 1999: Diurnal and semidiurnal variations in global surface winds and divergence fields. *J. Geophys. Res.*, **104**, 31 109–31 125.
- Gray, W. M., and R.W. Jacobson Jr., 1977: Diurnal variation of deep cumulus convection. *Mon. Wea. Rev.*, **105**, 1171–1188.
- Hahn, Douglas G. and Syukuro Manabe, 1975: The role of mountains in the South Asian monsoon circulation. *J. Atmos. Sci.*, **32**, 1515–1541.
- Holton, James R., *An Introduction to Dynamic Meteorology. Third Edition*, 511pp., Academic Press, Inc., San Diego, CA, 1992.
- Johnson, R. and P. Ciesielski, 1998: Preliminary results from the South China Sea monsoon experiment sounding network, *Proc. IX Pacific Science Inter-Congress, Asian Pacific Monsoon and Typhoon Meteorology Symp.*, Taipei, Taiwan, 65–66.
- Krishnamurti, T. N., C. M. Kishtawal, 2000: A pronounced continental-scale diurnal mode of the Asian summer monsoon. *Mon. Wea. Rev.*, **128**, 462–473.
- Krishnamurti, T.N. et al., 1981: On the onset vortex of the summer monsoon. *Mon. Wea. Rev.*, **109**, 344–363.
- Krishnamurti, T.N., 1979: Tropical Meteorology. *Compendium of Meteorology II*, WMO-no.364, Wiin-Nelson, Ed., World Meteorology Organization, 428 pp.
- Kummerow, C., et al., 2000: The Status of the tropical rainfall measuring mission (TRMM) after two years in orbit. *J of App. Met.* **39**, 1965–1982.
- Kummerow, C., et al., 1998: The Tropical Rainfall Measuring Mission (TRMM) Sensor Package.

- J Atmos. and Oceanic Tech.* **15**, 809–817.
- Lau, K.M., et. al., 1999: A report of the field operations and early results of the South China Sea monsoon experiment (SCSMEX), *Bull. Amer. Met. Soc.*, **81**, pp. 1261–1270.
- Lau, K.-M., H.-T. Wu, S. Yang, 1998: Hydrologic processes associated with the first transition of the Asian summer monsoon: A pilot satellite study. *Bull. Amer. Met. Soc.*, **79**, 1871–1882.
- Li, C., and J. Wu, 1999: On the onset Of the South China Sea summer monsoon in 1998. *Adv. in Atmos. Sci.*, **17**, 195–204.
- Lim, Gyu-Ho, A.-S. Suh, 2000: Diurnal and semidiurnal variations in the time series of 3-Hourly assimilated precipitation by NASA GEOS-1. *J. Climate*, **13**, 2923–2940.
- Loechl, E.M., 2001: Intraseasonal oscillations and the southeast Asian monsoon onset. Atmospheric Science Paper No. 703, Colorado State University, Fort Collins, Co., 123 pp.
- Molinari, J., S. Skubis, 1988: Calculation of consistent flux and advective terms from adjusted vertical profiles of divergence. *Mon. Wea. Rev.*, **116**, 1829–1837.
- Murakami, T., and Nakazawa, 1985: Transition from the southern to northern hemisphere summer monsoon. *Mon. Wea. Rev.*, **113**, 1470–1486.
- O'Brien, J. J., 1970: Alternative solutions to the classical vertical velocity problem. *J. App. Met.*, **9**, 197–203.
- Nuss, W. A., D. W. Titley, 1994: Use of multiquadric interpolation for meteorological objective analysis. *Mon. Wea. Rev.*, **122**, 1611–1631.
- Rao, Y.P., 1976: *Southwest Monsoon*. Meteor. Monogr., Synoptic Meteorology, India Meteorology Department, 376 pp.
- Riehl, H., and J. Simpson, 1979: The heat balance of the equatorial trough zone, revisited. *Atmos. Physics.*, **52**, 287–304.
- Ruprecht, E. and W. M. Gray, 1976a: Analysis of satelitte-observed tropical cloud clusters. I. Wind and dynamnic fields. *Tellus*, **28**, 392–413.

- Ruprecht, E. and W. M. Gray, 1976b: Analysis of satellite-observed tropical cloud clusters. II. Thermal moisture and precipitation. *Tellus*, **28**, 413–426.
- Schumacher, Courtney, Robert A. Houze Jr., 2000: Comparison of radar data from the TRMM satellite and Kwajalein oceanic validation site. *J. App. Met.*, **39**, 2151–2164.
- Wu, Guoxiong, Yongsheng Zhang, 1998: Tibetan plateau forcing and the timing of the monsoon onset over South Asia and the South China Sea. *Mon. Wea. Rev.*, **126**, 913–927
- Xu, K.-M., D. A. Randall, 1995: Impact of interactive radiative transfer on the macroscopic behavior of cumulus ensembles. Part II: Mechanisms for cloud-radiation interactions. *J. Atmos. Sci.*, **52**, 800–817.
- Xu, K.-M., D. A. Randall, 1995: Impact of interactive radiative transfer on the macroscopic behavior of cumulus ensembles. Part I: Radiation parameterization and sensitivity tests. *J. Atmos. Sci.*, **52**, 800–817.